

# Steady and unsteady non-Newtonian inelastic flows in a planar T-junction<sup>☆</sup>

H.M. Matos, P.J. Oliveira<sup>\*</sup>

Departamento de Engenharia Electromecânica, Universidade da Beira Interior, Rua Marques D'Avila e Bolama, 6201-001 Covilhã, Portugal

## ARTICLE INFO

### Article history:

Received 22 March 2012

Received in revised form 17 November 2012

Accepted 27 November 2012

Available online 25 December 2012

### Keywords:

T-junction flow

Non-Newtonian fluid

Carreau-Yasuda model

Hemodynamics

## ABSTRACT

Steady and unsteady laminar flows in a planar 2D T-junction, having a dividing or bifurcating flow arrangement (one main channel with a side branch at 90°), are studied numerically for non-Newtonian inelastic fluids whose rheological characteristics are similar to those of blood. These computational fluid dynamics simulations explore a wide range of variation of inertia (through the Reynolds number,  $Re$ ), flow rate ratio (proportion of extracted to inlet flow rates,  $\beta$ ) and shear thinning (the power-law index of the model,  $n$ ), and investigate their influence on the sizes and intensities of the recirculating eddies formed near the bifurcation, and on the resulting distribution of the shear stress fields. Such flow characteristics are relevant to hemodynamics, being related to the genesis and development of vascular diseases, like the formation of atherosclerotic plaques and thrombi near arterial bifurcations.

To represent the decay of viscosity with shear rate we apply the Carreau-Yasuda equation, one of the most utilized Generalized Newtonian Fluid model in blood simulations. In many comparisons of the present parametric study it was required that the level of inertia was kept approximately the same when  $n$  was varied. This implied a consistent definition of  $Re$  with the viscosity calculated at a representative shear rate.

© 2012 Elsevier Inc. All rights reserved.

## 1. Introduction

T-junction flows are of great importance in many situations in engineering and bio engineering applications. In engineering applications, many of the previous studies were mainly aimed to quantifying the pressure losses through the two branching arms in single-phase Newtonian (Costa et al., 2006) and two-phase flows (Doherty et al., 2009), or understanding the complex flow patterns resulting from 3D effects, as in hydraulic side-diversion channels (Neary and Sotiropoulos, 1996; Neary et al., 1999; Louda et al., 2011). More recent interest in microfluidics has revived the study of both T- and Y-junctions, an illustrative example being the experimental/numerical work of Balan et al. (2010). Bio engineering applications are well illustrated by the hemodynamical circulatory system, in which blood flows along successive levels of arterial bifurcations producing highly complex flow patterns that promote the appearance of regions with flow separation and recirculation. The relevance of numerical CFD investigation to hemodynamical flow bifurcations is granted by the known fact that the occurrence of cardiovascular diseases tends to be concentrated near the branches of arterial bifurcations (Ku et al., 1985; Debakey et al., 1985). These diseases are the major cause of premature death in

most European populations and are an important source of disability, contributing in large part to the escalating costs of health care (de Backer et al., 2003).

The most common manifestation of arterial disease is atherosclerosis which is now considered an inflammatory disease (Ross, 1999; Crowther, 2005). Since the location of atherosclerotic plaques tends to occur in regions of arterial bifurcations where the flow is very complex and possesses large shear stress gradients, both high and low shear stresses were initially considered to be the main contributor to the generation of the disease. Fry (1969) and Joris et al. (1982) have suggested that high shear stresses were more relevant in promoting the damage of the artery walls and thus facilitating the passage of blood constituents to the inside of the surrounding tissues. On the other hand Caro et al. (1971) offered a different explanation and have implied that it is in areas of arterial walls where the mean shear stresses are low and where in addition the velocities are also reduced, like in recirculation zones, that the development of atheromas are predisposed, because the residence time of blood cells in these places is longer and allows for their adhesion and displacement to the endothelium wall, initiating an atherosclerotic plaque formation. Several subsequent studies have tried to decide on which of these theories was valid. Zarins et al. (1983) and Ku et al. (1985) confirmed the observations of Caro et al. (1971) and showed that there exists a definite tendency for the occurrence of atherosclerotic lesions in areas where shear stresses have low magnitudes.

<sup>☆</sup> Research Units: UMTF (Covilhã) and CEFT (Porto).

<sup>\*</sup> Corresponding author.

E-mail addresses: [heldermiguelmm@hotmail.com](mailto:heldermiguelmm@hotmail.com) (H.M. Matos), [jpjo@ubi.pt](mailto:jpjo@ubi.pt) (P.J. Oliveira).

However more recent studies, like [Berger and Jou \(2000\)](#) for example, indicate that both the spatial and the temporal wall shear stress gradients are more relevant than their magnitudes to correlate with atherosclerotic plaques location. In laminar flows the endothelial cells are aligned with the flow direction, while areas of disturbed flow where the shear stress is oscillatory do not have a definite orientation and a strong organization of those cells ([Chien, 2008](#)), thus stimulating the inflammatory process ([Cunningham and Gotlieb, 2005](#)), which increases the macromolecules permeability and migration into the arterial wall ([Hsiai et al., 2003](#)), and leading finally to the atherosclerotic plaque formation ([Crowther, 2005](#)).

Since the process of atherosclerotic plaque formation is directly related to the existence of oscillatory shear stress, the numerical investigation of unsteady blood flows in arterial bifurcations is essential for a better understanding of its genesis. An important aspect here is to have fundamental knowledge on the behaviour of the recirculation eddies, which are generated by the flow distribution in the bifurcation area and are characterized by low shear stresses in their interior, while high shear stresses develop in the boundary separating them from the main flow. Such combination leads to large stress gradients and high local oscillations of their magnitudes in space and time when the recirculation sizes vary with inertia, flow rate ratio, time or other variable.

Blood is a non-Newtonian fluid showing a shear-thinning viscosity and, in small blood vessels where the shear rates are commonly lower than  $50 \text{ s}^{-1}$  ([Stuart and Kenny, 1980](#)), it is also thixotropic and viscoelastic ([Owens, 2006; Miranda et al., 2008](#)). In large blood vessels where the shear rates are higher, blood can be modelled as a Newtonian fluid, typically for shear rates above  $500 \text{ s}^{-1}$  ([Long et al., 2005](#)). Recent numerical works involving simulations of vascular dynamics in branching flows where blood was considered a Newtonian fluid are exemplified by the studies of [Tsui and Lu \(2006\)](#), in symmetrical Y and T bifurcations, and [Chitra et al. \(2009\)](#), in more complex cavo-pulmonary connections (having 2 entries and 4 exits).

The present paper is targeted to the study of non-Newtonian shear thinning viscosity effects on the flow through a planar T-junction, while the viscoelastic effects are planned for a future study. An earlier contribution which served as a motivation for our study was the work of [Miranda et al. \(2008\)](#), who essentially looked to steady and periodic flows of Newtonian fluids through a similar bifurcation geometry and obtained results in close agreement with previous experimental measurements and also with simulations of [Liepsch et al. \(1982\)](#), [Khodadadi et al. \(1986, 1988\)](#) and [Khodadadi \(1991\)](#). In particular, their results for the size and intensity of the recirculation zones formed near the bifurcation have controlled accuracy and may be considered benchmark data; [Moshkin and Yambangwi \(2009\)](#) have replicated some of that data in a numerical study where the purpose was to implement pressure boundary-conditions at outlets, instead of the flow rate split that we impose. [Miranda et al. \(2008\)](#) examined a single case of non-Newtonian flow and left open a route of investigation dealing with the analysis of other fluid characteristics, such as the level of shear-thinning, upon the flow patterns around the bifurcation.

Two dimensional simulations are deemed adequate to represent actual 3D situations when the aspect ratios of the ducts forming the T-junction are large, as in the experiments of [Liepsch et al. \(1982\)](#) and [Khodadadi et al. \(1986\)](#) mentioned above for which the aspect ratio was 8 (depth:width = 80 mm:10 mm).

In comparison with the work of [Miranda et al. \(2008\)](#) that precedes this one, we looked into the influences of inertia ( $50 \leq Re \leq 1000$ , with steps of 50), flow rate ratio ( $0.1 \leq \beta \leq 0.9$ , with steps of 0.1) and shear thinning ( $0.1 \leq n \leq 1.0$ , with steps of 0.1). More precisely, when considering a constant flow rate ratio, its value was taken as  $\beta = 0.7$  and the Reynolds number was varied

for a range of values (0–1000), and when considering constant inertia, the Reynolds number was  $Re = 102$  and the flow rate ratio  $\beta$  was varied from 0.1 to 0.9. Regarding the unsteady simulations, inertia was kept constant at the standard value  $Re = 102$ , like in [Khodadadi \(1991\)](#) and [Miranda et al. \(2008\)](#), and shear thinning was varied at constant flow rate ratio ( $\beta = 0.7$ ), while this parameter  $\beta$  was varied at constant shear thinning ( $n = 0.3568$ ).

The simulations with Newtonian fluids are compared to simulations with non-Newtonian cases at a given Reynolds number obtained under a consistent manner in order to keep inertia effectively constant. In this way it was possible to reach definite conclusions on the competing effects of inertia, shear thinning and extraction ratio for either Newtonian or non-Newtonian flows in the T-junction.

## 2. Governing equations

For the simulation of incompressible and isothermal, laminar, time-dependent flows, the equations to be solved are those expressing conservation of mass (Eq. (1)) and of linear momentum (Eq. (2)):

$$\nabla \cdot \mathbf{u} = 0 \quad (1)$$

$$\rho \left( \frac{\partial \mathbf{u}}{\partial t} + \nabla \cdot (\mathbf{u}\mathbf{u}) \right) = -\nabla p + \nabla \cdot \boldsymbol{\tau} \quad (2)$$

where  $\mathbf{u}$  is the velocity vector,  $p$  is the pressure,  $\rho$  is the fluid density (constant) and  $\boldsymbol{\tau}$  is the stress tensor. The stress tensor in Eq. (2) is specified by a rheological constitutive model which depends on whether the fluid is Newtonian or non-Newtonian (inelastic).

For Newtonian fluids the stress tensor follows the Newton law for viscosity expressing a linear and explicit stress-strain rate relationship

$$\boldsymbol{\tau} = \eta_N \dot{\boldsymbol{\gamma}} \quad (3)$$

where  $\dot{\boldsymbol{\gamma}} = (\nabla \mathbf{u} + \nabla \mathbf{u}^T)$  is the shear rate tensor and  $\eta_N$  is the Newtonian fluid viscosity ( $\eta_N = 0.0084 \text{ Pa s}$ , to replicate the experiments of [Khodadadi et al. \(1988\)](#); the important point is that this viscosity gives  $Re = 102$  for the base case, as in [Miranda et al., 2008](#)). For non-Newtonian inelastic fluids the viscosity  $\eta$  is a function of shear rate magnitude ( $\dot{\gamma} = |\dot{\boldsymbol{\gamma}}| = \sqrt{\frac{1}{2} \dot{\boldsymbol{\gamma}} : \dot{\boldsymbol{\gamma}}}$ ) and Generalized Newtonian Fluids (GNF) were used to express the rheological constitutive equation:

$$\boldsymbol{\tau} = \eta(\dot{\gamma}) \dot{\boldsymbol{\gamma}} \quad (4)$$

In the latter case the Carreau-Yasuda equation ([Yasuda et al., 1981](#)) is chosen as a model to represent the viscosity variation with shear rate:

$$\eta = \eta_\infty + (\eta_0 - \eta_\infty) [1 + (\lambda \dot{\gamma})^a]^{\frac{n-1}{a}} \quad (5)$$

In Eq. (5),  $\eta_0$  and  $\eta_\infty$  are the zero and infinite shear rate viscosities,  $\lambda$  is a time constant representing the inverse of the shear rate at which the viscosity starts decreasing,  $n$  is the power law exponent (when  $n = 1$  the fluid is Newtonian and  $\eta = \eta_0$ ) and the parameter  $a$  represents the width of the transition region between  $\eta_0$  and the power-law region. The values assigned to these parameters expressing the fluid viscosity (Table 1) are the same as in the rheological model followed by [Banerjee et al. \(1997\)](#) who adjusted the Carreau-Yasuda model to the experimental curves of viscosity of blood versus shear rate published by [Cho and Kensey \(1991\)](#).

Although the zero shear rate viscosity of the Carreau-Yasuda model defined in Table 1 is different from the Newtonian viscosity  $\eta_N$  used in this work, and in previous works which served as the basis for the present study ([Khodadadi et al., 1988; Khodadadi, 1991; Miranda et al., 2008](#)), it is worth realizing that under what

**Table 1**  
Parameters of Carreau-Yasuda model for blood (Banerjee et al., 1997).

Parameter	
Power law exponent ( $n$ )	0.3568
Carreau parameter ( $a$ )	2
Zero-shear viscosity ( $\eta_0$ )	0.056 Pa s
Infinite-shear viscosity ( $\eta_\infty$ )	0.00345 Pa s
Time constant ( $\lambda$ )	3.313 s

were taken as the standard conditions in the cited works (namely:  $Re = 102$  and  $\beta = 0.7$ ), the viscosity obtained through the Carreau-Yasuda model after the calculation of the mean shear rate, as the ratio between the mean velocity ( $\bar{u}_1 = 0.0745$  m/s for  $Re = 102$  in a Newtonian flow) and the half height of the channel ( $\dot{\gamma}_1 = \bar{u}_1/(0.5H)$ ), are similar. In fact, at the inlet  $\dot{\gamma}_1 = \bar{u}_1/(0.5H) = 14.9$  s<sup>-1</sup>, with which is possible to obtain a viscosity  $\eta_1 = 0.00773$  Pa s using Eq. (5) for the Carreau-Yasuda model. At the outlet in the secondary branch  $\dot{\gamma}_3 = \bar{u}_3/(0.5H) = 10.4$  s<sup>-1</sup> and  $\eta_3 = 0.00883$  Pa s. These values of viscosity are close to the Newtonian viscosity here employed ( $\eta_N = 0.0084$  Pa s) leading to comparable results for the Newtonian and non-Newtonian cases.

### 3. Numerical method

The partial differential equations of the previous section (Eqs. (1)–(4)) are discretized using the finite-volume method (e.g. Ferziger and Peric, 2002), after being integrated in space over the set of control volumes (cells, size  $\Delta x$ ) forming the computational mesh, and integrated in time over the finite time intervals or time steps (denoted by  $\Delta t$ ). This procedure results in several sets of linearised algebraic equations, one for each independent variable ( $\mathbf{u}$ ,  $p$ ,  $\tau$ ). In the present implementation all variables are stored at the centre of the control volumes, the so-called collocated mesh arrangement which requires special procedures to ensure adequate coupling between the velocity and the pressure fields. This goal is guaranteed through a particular technique based on the Rhie and Chow (1983) interpolation method which permits to achieve solutions independent of the time step value for steady state flows (Issa and Oliveira, 1994). On the other hand the coupling between the velocity and stress fields is obtained through a similar technique developed by Oliveira et al. (1998), Oliveira and Pinho (1999), and later modified by Matos et al. (2009) in order to produce  $\Delta t$ -independent results, similarly to the velocity/pressure coupling just mentioned.

The present version of the numerical method (Issa and Oliveira, 1994) employs general coordinates and indirect-addressing for easy mapping of non-rectangular domains, such as the T-junction domain here considered, together with the non-staggered mesh arrangement.

The diffusive and the pressure gradient terms in the governing equations are represented by central differences (having second-order accuracy) while the convective terms are approximated by the high resolution scheme CUBISTA of Alves et al. (2003), with third-order accuracy in space for smooth flow and thus combining relatively high numerical precision with better iterative convergence characteristics. For the temporal discretisation of the unsteady terms we apply the three-time level scheme described, among others, by Oliveira (2001) which results in a discretization scheme also formally possessing second-order accuracy.

The discretised sets of equations are solved iteratively and sequentially using an algorithm based on the SIMPLEC of Van Doormaal and Raithby (1984) that allows, through an iterative pressure correction procedure, the coupling of the velocity and pressure fields, in order to verify the continuity equation. In relation to the original SIMPLEC algorithm, the present algorithm is

able to simulate transient flows on non-staggered meshes, using the time marching procedure described by Issa and Oliveira (1994), which can be used also in steady flows as an alternative to implement under-relaxation. Subsequently Oliveira et al. (1998) included modifications in order to deal with the stress constitutive equations of non-Newtonian viscoelastic flows.

Convergence of the iterative, time-marching process is obtained when the normalized residuals of all variables are less than  $10^{-8}$ .

### 4. Geometry, computational meshes and accuracy tests

The numerical simulations were carried out in a bifurcation geometry having the shape of a T-junction (Fig. 1). It has a constant and rectangular cross-sectional area, with the height of the channels being  $H = 0.01$  m and the origin of the coordinate axes are located at the central position in the bifurcation zone.

The minimum lengths of the bifurcation channels that guaranty a fully developed flow at the outlets depend on the flow characteristics and are obtained according to Shah and London (1978):

$$\frac{L}{H} = \frac{0.315}{0.068 Re + 1} + 0.044 Re \quad (6)$$

This expression is only valid for Newtonian flows but it helps in estimating the required geometry dimensions. The Reynolds number in Eq. (6), which is also used later when varying the flow inertia, is defined as:

$$Re = \frac{\rho \bar{u}_1 H}{\eta} \quad (7)$$

where  $\bar{u}_1$  is the mean velocity at the inlet,  $\rho$  is the fluid density ( $\rho = 1150$  kg/m<sup>3</sup>) and  $\eta$  is the fluid viscosity. This viscosity is unambiguous for the Newtonian fluid ( $\eta_N = 0.0084$  Pa s) but requires further discussion in relation to the Carreau-Yasuda model of Eq. (5), a matter which is postponed to later in this section.

For either a maximum Reynolds number of 1000 or a typical value of 102 the channel lengths obtained through the Shah and London expression are respectively  $L_2 = L_3 = 44H$  and  $L_2 = L_3 = 4.5H$ . However, to be on the safe side and since the Shah and London expression was only established for Newtonian flows, the channel lengths were extended to  $L_2 = L_3 = 59.5H$  for the large  $Re$  cases (namely for  $Re$  close to 1000), while the values  $L_2 = 22H$  and  $L_3 = 20H$ , already used in previous studies (Miranda et al., 2008; Matos et al., 2009), were maintained for the base case  $Re = 102$ . Similarly, based on those previous works, the inlet duct length was  $L_1 = 3.0H$  at  $Re = 102$  while for flows with higher inertia we used  $L_1 = 6H$ . We have checked that these assumed inlet lengths yield results which are almost independent of the particular value of  $L_1$ , especially regarding the non-Newtonian cases for which the inlet velocity profile is not exactly the same as the fully-developed Newtonian solution (no exact solution is known for these cases). When the Reynolds number is 500 and the power law exponent is 0.3568, the recirculation lengths vary by only 0.8% when  $L_1$  is changed from  $L_1 = 6H$  to  $L_1 = 12H$ . Other cases tested exhibit a variation smaller than about 1.2% and therefore we can define  $L_1 = 6H$  as an adequate inlet duct length.

In the present simulation there are three types of boundary conditions: inlets, outlets and solid walls. On the solid walls the no slip boundary condition was imposed and the stresses were obtained from local analytical expressions.

At the outlets, located at  $x = 22.5H$  and  $y = 20.5H$ , or  $x = 60H$  and  $y = 60H$ , depending on the outlet channel lengths, Neumann boundary conditions were used, forcing vanishing axial variation for all variables (i.e.  $\partial/\partial x = 0$  in the horizontal duct and  $\partial/\partial y = 0$  in the vertical duct), except pressure, for which a constant gradient was assumed and the boundary value obtained by linear extrapolation from inside.

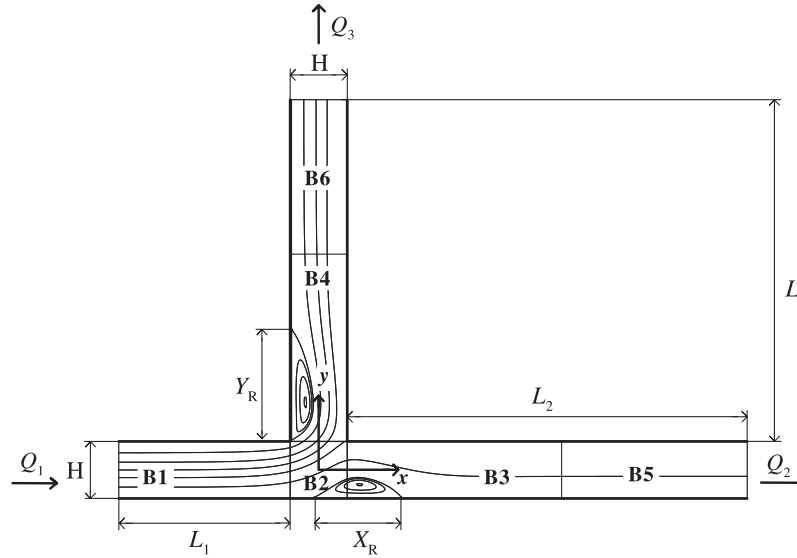


Fig. 1. Bifurcation geometry.

At the inlet ( $x = -3.5H$  or  $x = -6.5H$ ), Dirichlet boundary conditions were used, by imposing a parabolic velocity profile for the steady state flows, while for transient flows the velocity profile is pulsating and generated by a sinusoidal pressure gradient that, as in Khodadadi et al. (1988) and Miranda et al. (2008), is given by:

$$-\frac{dp}{dx} = \rho K_S + \rho K_O \cos(\omega t) \quad (8)$$

Here  $\rho K_S$  is the magnitude of the steady pressure gradient and  $\rho K_O = 190 \text{ Pa/m}$  is the magnitude of the oscillating pressure gradient. For the base case of  $Re = 102$ , the steady mean velocity is  $\bar{u}_1 = 0.0745 \text{ m/s}$  which corresponds to a steady pressure gradient of  $\rho K_S = 75.1 \text{ Pa/m}$  ( $\bar{u}_1 = \rho K_S H^2 / 12 \eta_N$ ). In fact the nondimensional parameter of interest is the ratio of oscillating and steady pressure gradients, given by  $K_O/K_S = 2.530$ , and the other relevant nondimensional parameter characterising the oscillating frequency is the Womersley number, defined as  $\alpha = (\frac{1}{2} H (\rho \omega / \eta)^{1/2}) = 4.864$ , a value typical of hemodynamical situations (frequency of  $f = 1.1 \text{ s}^{-1}$ ). In engineering applications, an imposed or a naturally-arising frequency is usually scaled with the typical time scale of the flow, and instead of the Womersley number it is more common to define a Strouhal number, as  $St = fL/U$ , which in the present case, by adopting the averaged inlet velocity and the duct height as velocity and length scales, gives  $St = fH/\bar{u}_1 = 0.15$ . This value is typical of, for example, vortex shedding from a cylinder at low Reynolds number, and therefore the present time-dependent periodic results may also be of interest to some engineering situations. In viscoelastic applications it is also possible to define an elastic number, as  $\lambda/T_{flow}$ , which gives here, using the time scale of the Carreau model,  $\lambda/T = \lambda f = 3.64$ ; this would represent a relatively high elasticity, although the GNF are inelastic models and the  $\lambda$  of Table 1 cannot be viewed as a measure of the fluid relaxation time.

For bifurcating flows an extra boundary condition is needed to express the ratio of flow rates going into each bifurcation arm, otherwise it is not possible to obtain a unique solution to the flow problem defined by the above equations and boundary conditions. The flow rate ratio is imposed directly in the algorithm and expresses the percentage of fluid in the secondary branch:

$$\beta = \frac{Q_3}{Q_1} \quad (9)$$

where  $Q_1$  and  $Q_3$  are respectively the volumetric flow rates at the inlet branch and at the secondary outlet branch, as represented in Fig. 1. In addition  $Q_2$  is the volumetric flow rate at the main outlet branch, with overall mass conservation giving  $Q_1 = Q_2 + Q_3$ .

The meshes are orthogonal but non-uniform, with increased concentration of cells near the bifurcation zone where the stress gradients are expected to be higher. For a better distribution of the mesh nodes over the computational domain the bifurcation geometry is created by the six structured blocks (B1–B6) which are identified in Fig. 1.

Tables 2 and 3 provide the main characteristics of the base meshes used in the simulations. Mesh M2 has 12800 control volumes and was employed in the studies with  $Re = 102$ ; mesh M5 has 22400 control volumes and was employed for the high  $Re$  cases, which needed longer branch arms, as discussed before.

Selection of those two meshes (M2 and M5) was guided by a study of mesh convergence based on simulations using three meshes with progressive degree of refinement. In order to have a consistent level of refinement, the finer mesh is obtained from the previous coarser mesh by doubling the number of cells along each direction and using the square-root of the corresponding expansion/contraction ratios ( $r_x$  and  $r_y$ ) inside each block. According to these conditions the coarser mesh (M1) associated with

**Table 2**  
Main characteristics of mesh M2.

Block	No. of cells $NX \times NY$	Size X	Size Y	$r_x$	$r_y$
B1	$40 \times 40$	$-3.5 \rightarrow -0.5$	$-0.5 \rightarrow +0.5$	0.95260	1.00000
B2	$40 \times 40$	$-0.5 \rightarrow +0.5$	$-0.5 \rightarrow +0.5$	1.00000	1.00000
B3	$100 \times 40$	$0.5 \rightarrow 12.5$	$-0.5 \rightarrow +0.5$	1.02657	1.00000
B4	$40 \times 100$	$-0.5 \rightarrow +0.5$	$0.5 \rightarrow 10.5$	1.00000	1.02385
B5	$20 \times 40$	$12.5 \rightarrow 22.5$	$-0.5 \rightarrow +0.5$	1.06413	1.00000
B6	$40 \times 20$	$-0.5 \rightarrow +0.5$	$10.5 \rightarrow 20.5$	1.00000	1.06413



**Table 3**  
Main characteristics of mesh M5.

Block	No. of cells $NX \times NY$	Size $X$	Size $Y$	$r_x$	$r_y$
B1	$80 \times 40$	$-6.5 \rightarrow -0.5$	$-0.5 \rightarrow +0.5$	0.9763	1.00000
B2	$40 \times 40$	$-0.5 \rightarrow +0.5$	$-0.5 \rightarrow +0.5$	1.0000	1.00000
B3	$100 \times 40$	$0.5 \rightarrow 10.5$	$-0.5 \rightarrow +0.5$	1.0238	1.00000
B4	$40 \times 100$	$-0.5 \rightarrow +0.5$	$0.5 \rightarrow 10.5$	1.0000	1.02385
B5	$120 \times 40$	$10.5 \rightarrow 60.0$	$-0.5 \rightarrow +0.5$	1.0073	1.00000
B6	$40 \times 120$	$-0.5 \rightarrow +0.5$	$10.5 \rightarrow 60.0$	1.0000	1.00730

**Table 4**  
Summary of the mesh convergence results for the shorter arms T-junction geometry (Newtonian fluid).

	$\beta = 0.7$ and $Re = 102$	
	$X_R$	$Y_R$
Mesh M1	1.52410	1.90309
Mesh M2	1.53367	1.95232
Mesh M3	1.53475	1.96689
$p$	3.15	1.76
$\phi_{extr}$	1.53489	1.97301
$\varepsilon_{4h}$ (M1)	0.70%	3.54%
$\varepsilon_{2h}$ (M2)	0.079%	1.05%
$\varepsilon_h$ (M3)	0.0091%	0.31%

M2 has 3200 control volumes, and the finest M3 has 51200 control volumes; similarly, the coarser mesh (M4) associated with M5 has 5600 control volumes and the finest M6 has 89600 control volumes.

With the procedure described in last paragraph it is easier to apply Richardson extrapolation technique which allows the calculation of the order of convergence of the method ( $p$ ) and estimation of a more accurate solution. The order of convergence of the method is given by (see e.g. Ferziger and Peric, 2002):

$$p = \frac{\log\left(\frac{\phi_{2h} - \phi_{4h}}{\phi_h - \phi_{2h}}\right)}{\log 2} \quad (10)$$

where  $\phi_{4h}$ ,  $\phi_{2h}$  and  $\phi_h$  are the solutions obtained with meshes M1, M2 and M3, or M4, M5 and M6, respectively. A more accurate, extrapolated solution can be obtained through the following expression (Ferziger and Peric, 2002):

$$\phi_{extr} \approx \phi_h + \varepsilon_h = \phi_h + \frac{\phi_h - \phi_{2h}}{2^p - 1} \quad (11)$$

where  $\varepsilon_h$  is the estimated error on the most refined mesh (M3 or M6).

The mesh convergence study is carried out by looking into the discretisation errors involved in the calculated horizontal and vertical recirculation lengths. Horizontal and vertical recirculating bubbles are created in the main and secondary branches, as represented in Fig. 1, where the respective lengths are denoted by  $X_R$  and  $Y_R$ . The recirculation starts when wall flow separation occurs and that is identified numerically by an inversion of sign in the horizontal or vertical velocity components along the wall; the end of the recirculations is assumed to occur when the flow reattaches and, again, the velocity component adjacent to the wall presents an inversion of sign. The separation and reattachment points are denoted by  $X_s$ ,  $Y_s$  and  $X_r$ ,  $Y_r$  and the recirculation lengths ( $X_R$ ,  $Y_R$ ) were obtained by their difference.

The mesh convergence results for the flows in the shorter-arms geometry are summarized in Table 4, corresponding to a Newtonian case at a flow rate ratio of  $\beta = 0.7$  and Reynolds number of  $Re = 102$  as in the previous study of Matos et al. (2009). For flows

**Table 5**  
Summary of the mesh convergence results for the longer arms T-junction geometry (non-Newtonian fluid).

	$\beta = 0.8$ and $Re = 102$		$\beta = 0.8$ and $Re = 500$	
	$X_R$	$Y_R$	$X_R$	$Y_R$
Mesh M4	1.34842	2.29277	6.96058	5.71957
Mesh M5	1.38309	2.42679	7.89595	8.05480
Mesh M6	1.39610	2.45732	8.08300	8.46143
$p$	1.41	2.138	2.32	2.52
$\phi_{extr}$	1.40391	2.46632	8.12976	8.54716
$\varepsilon_{4h}$ (M4)	3.95%	7.04%	14.38%	33.08%
$\varepsilon_{2h}$ (M5)	1.48%	1.60%	2.88%	5.76%
$\varepsilon_h$ (M6)	0.56%	0.36%	0.58%	1.00%

at larger Reynolds numbers the longer-arms geometry is employed and the results of the mesh convergence study are presented in Table 5, for two Reynolds numbers ( $Re = 102$  and  $Re = 500$ ), a flow rate ratio of  $\beta = 0.8$ , and the non-Newtonian inelastic fluid that follows the Carreau-Yasuda model whose parameters are given in Table 1. In particular Tables 4 and 5 show the extrapolated, more accurate solution obtained with Eq. (11) and the order of convergence obtained with Eq. (10).

The results given in Tables 4 and 5 show the proximity of the solutions obtained with the intermediate meshes M2 and M5 to the reference solutions obtained through the Richardson's extrapolation technique, demonstrating errors smaller than 2% for  $Re = 102$ , and smaller than 6% for  $Re = 500$ , and thus allowing the conclusion that M2 and M5 provide a good compromise between the accuracy of results and the time required for solution convergence.

In addition to the accuracy of the mesh convergence study presented, if the three meshes used are sufficiently refined the behaviour of the solution error with mesh refinement must present a linear decay in a logarithmic scale, such as it is visible for all the cases analysed, which are represented in Fig. 2.

#### 4.1. Definition of effective Reynolds number

The Reynolds number used up to this point was calculated under Newtonian flow conditions, following Eq. (7) with  $\eta = \eta_N$  even when the fluid is non-Newtonian. For Newtonian fluids the viscosity does not change and the Reynolds number variation is solely obtained by changing the fluid mean velocity at the inlet, since  $\rho$  and  $H$  are also constant. However, for non-Newtonian fluids viscosity depends on the shear rate and that affects the Reynolds number, producing a hidden variation of the Reynolds number and wrong comparison between Newtonian and non-Newtonian cases when this variation is not taken in consideration. The problem of adequate dynamic scaling of non-Newtonian fluid flow is not a simple one, depending not only on the geometry and the corresponding typical shear rates, but also on the rheological model; the analysis of Gray et al. (2007) is relevant here, as the choice taken by Escudier et al. (2002) in axial annular flow with and without rotation of the inner cylinder.

The differences encountered can be quite large when one intends to analyse shear thinning effects: an actual Reynolds number of 150 for  $n = 1$  drops down to  $Re \approx 15$  for  $n = 0.1$ , while the standard case is  $Re = 102$  for  $n = 0.3568$ . These results are based on the parameters of Table 1 which remain unchanged when  $n$  is varied.

It is therefore clear that, in order to perform an exclusive analysis of shear thinning through the variation of the power law exponent, it is necessary to maintain unaltered the effective Reynolds number, for all cases considered. Since in the Reynolds number equation (Eq. (7))  $\rho$  and  $H$  are fixed, for non-Newtonian fluids  $Re$

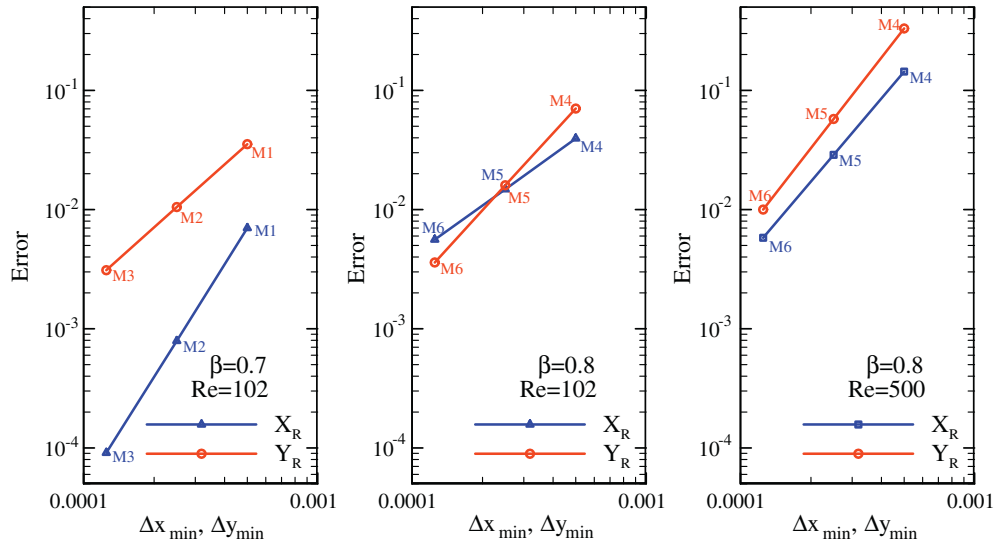


Fig. 2. Variation of solution error with mesh refinement.

can be varied either through the mean velocity at the inlet or the viscosity, which is a function of shear rate, as defined by the Carreau-Yasuda model.

Hence, we may envisage two options to evaluate the Reynolds number in a consistent manner, so that inertial effects are kept unchanged between the Newtonian and the non-Newtonian cases. In both methods the Reynolds number should be calculated by an expression similar to Eq. (7), except that now, since viscosity varies with shear rate  $\eta(\dot{\gamma})$ , a characteristic shear rate must be specified, thus:

$$Re = \frac{\rho \bar{u}_1 H}{\eta(\dot{\gamma}_1)} \quad \text{with} \quad \dot{\gamma}_1 = \frac{\bar{u}_1}{H/2} \quad (12)$$

The first option consists in an iterative procedure to determine the mean velocity that the flow must have at the inlet section, for a specified Reynolds number  $Re$ , when the corresponding viscosity of the fluid is obtained from the Carreau-Yasuda model, based on the characteristic shear rate, and all parameters in Table 1 are kept unchanged, except the power law exponent which may be varied when the shear thinning intensity is intentionally changed:

$$\bar{u}_1 = \frac{Re}{\rho H} \left( \eta_\infty + (\eta_0 - \eta_\infty) [1 + (\lambda 2 \bar{u}_1 / H)^a]^{n-1} \right) \quad (13)$$

This equation is iterated until  $\bar{u}_1$  attains an unchanging value.

The second option consists in keeping the mean velocity and viscosity identical to the mean velocity and viscosity of the Newtonian case, and consequently forcing the Reynolds number to remain constant. In order to maintain the viscosity constant with a variation of the power law exponent it is necessary to change the magnitude of the other parameters involved in its calculation inside the Carreau-Yasuda model. The parameter selected to change was the value of the zero shear rate viscosity ( $\eta_0$ ), which is calculated from:

$$\eta_0 = \eta_\infty + (\rho \bar{u}_1 H / Re - \eta_\infty) / [1 + (\lambda 2 \bar{u}_1 / H)^a]^{n-1} \quad (14)$$

In this paper, besides the analysis of the effects of inertia ( $Re$ ), flow rate ratio ( $\beta$ ) and shear thinning ( $n$ ) on steady and unsteady flows, we also wish to compare Newtonian and non-Newtonian fluid behaviour and, in the later case, the comparison is made using a definition for  $Re$  based on either Newtonian conditions or in the more consistent, and realistic way, which maintains inertia constant between the several fluids. For future identification, we refer

to the “Newtonian Reynolds method” or  $Re_{Newt}$ , when  $Re = \rho \bar{u}_1 H / \eta_N$  with  $\eta_N = 0.0084$  Pa s, and to “Modified Reynolds method” or  $Re_{Mod}$ , when  $Re = \rho \bar{u}_1 H / \eta(\dot{\gamma}_1)$  with  $\dot{\gamma}_1 = \bar{u}_1 / (0.5H)$  and  $\eta(\dot{\gamma}_1)$  obtained from Eq. (5) where the Carreau-Yasuda model parameters are given in Table 1.

## 5. Results and discussion

The results presented are normalised, using as length scale the channels height  $H$  ( $Y = y/H$  and  $X = x/H$ ), as velocity scale the average velocity of the inlet flow ( $\bar{u}_1$ ), as stress scale the value of the wall shear stress at inlet under fully-developed steady flow ( $\tau_{w1} = 6\eta \bar{u}_1 / H$ ), and the ratio  $2\pi/\omega$  for time scale. In the stress scale the characteristic viscosity depends on the fluid; for Newtonian and GNF fluids with the Newtonian Reynolds method, the Newtonian viscosity is used  $\eta_N = 0.0084$  Pa s, while for GNF fluids with the Modified Reynolds method the viscosity is obtained from the Carreau-Yasuda model at  $\dot{\gamma}_1 = \bar{u}_1 / (0.5H)$ . It is noted that  $\tau_{w1}$  is not exactly equal to the wall shear stress for the non-Newtonian fluid; this small discrepancy may produce slightly imperfect comparisons.

The results are presented and discussed in two sections. Section 5.1 deals with steady-state laminar flow, focusing on the influence of inertia, flow rate ratio and shear-thinning upon the main flow characteristics, namely the size and intensity of the eddies formed near the flow division, and the shear stress fields. The non-Newtonian fluids are characterized with the parameters of Table 1 for a Carreau-Yasuda model, and the variation of shear-thinning is accomplished at (i) a constant flow rate ratio and variable Reynolds number; or (ii) a constant Reynolds number and variable flow rate ratio. Section 5.2 deals with a similar study for time-varying periodic flows, but the Reynolds number is kept constant.

### 5.1. Non-Newtonian inelastic steady-state flows

These results are presented in two sub-sections: the first (Section 5.1.1) is focused on the influence of varying inertia and flow rate ratio, and looking into the main flow characteristics; the second (Section 5.1.2) deals with the effect of shear thinning, looking simultaneously to (i) the influence of inertia at constant flow rate ratio, and (ii) the influence of flow rate ratio at constant Reynolds number.

### 5.1.1. Inertia and flow rate ratio variation (constant shear thinning)

Bifurcation flows are characterized by the existence of two main recirculations, one on each arm, along the  $x$  and  $y$  directions, also referred to here as horizontal and vertical directions. The size of the two recirculating eddies is characterised by their length, which was obtained from the velocity profiles parallel and adjacent to the horizontal ( $Y = -0.5$ ) and vertical ( $X = -0.5$ ) walls; changes in sign of the horizontal and vertical velocity components, correspond to the separation and reattachment points of the recirculating flow, that is, the beginning and the ending points of the eddy.

Figs. 3 and 4 give the results predicted for the length of the recirculation eddies in the main channel (Fig. 3) and in the secondary branch (Fig. 4), with increasing inertia and flow rate ratio. In both figures, the three graphs on the left (a, b, c) present the variation of the recirculation lengths with inertia and flow rate ratio, as a parameter, for the Newtonian case, the non-Newtonian fluid (GNF  $n = 0.3568$ ) with  $Re$  from the Newtonian Reynolds method, and the same GNF fluid with  $Re$  based on the Modified Reynolds method. The graphs on the right (d, e, f) make a more direct comparison between results for Newtonian and non-Newtonian fluids for three specific values of extraction ratio ( $\beta = 0.2, 0.5$  and  $0.8$ ).

The first aspect to note in either Figs. 3 or 4 is the monotonic increase of recirculation eddy length with the Reynolds number, for

both horizontal and vertical recirculations. The horizontal branch eddy increases linearly with Reynolds number for flow rate ratios lower than  $0.8$ , while for higher values of extraction ratio and for all cases in what regards the eddy in the vertical branch, the linear behaviour ceases to exist. In fact, for the vertical recirculation there is a very clear reduction in growth rate above a certain Reynolds number, which is more evident at moderate and high flow rate ratio. This feature may be explained by the interaction of the main vertical recirculation with a new recirculation formed immediately downstream, on the opposite side wall of the secondary branch, which acts as to squeeze the first eddy and delay its growth.

Inspection of the left plots in Figs. 3 and 4a–c also reveals the influence of flow rate ratio: starting with  $\beta = 0$ , both the horizontal and vertical recirculation lengths increase with flow rate ratio, irrespective of  $Re$ , up to a maximum size when the extraction ratio attains  $\beta = 0.6$  and, for higher values of extraction, the size of the eddies decrease.

On the other hand, inspection of the plots on the right of Figs. 3 and 4d–f facilitates the comparison between the two types of fluid, and large discrepancies are seen between the results for the GNF fluid with the Newtonian Reynolds method and the other two sets of results. In general, the Newtonian Reynolds method yields much larger recirculation lengths, especially so for high values of

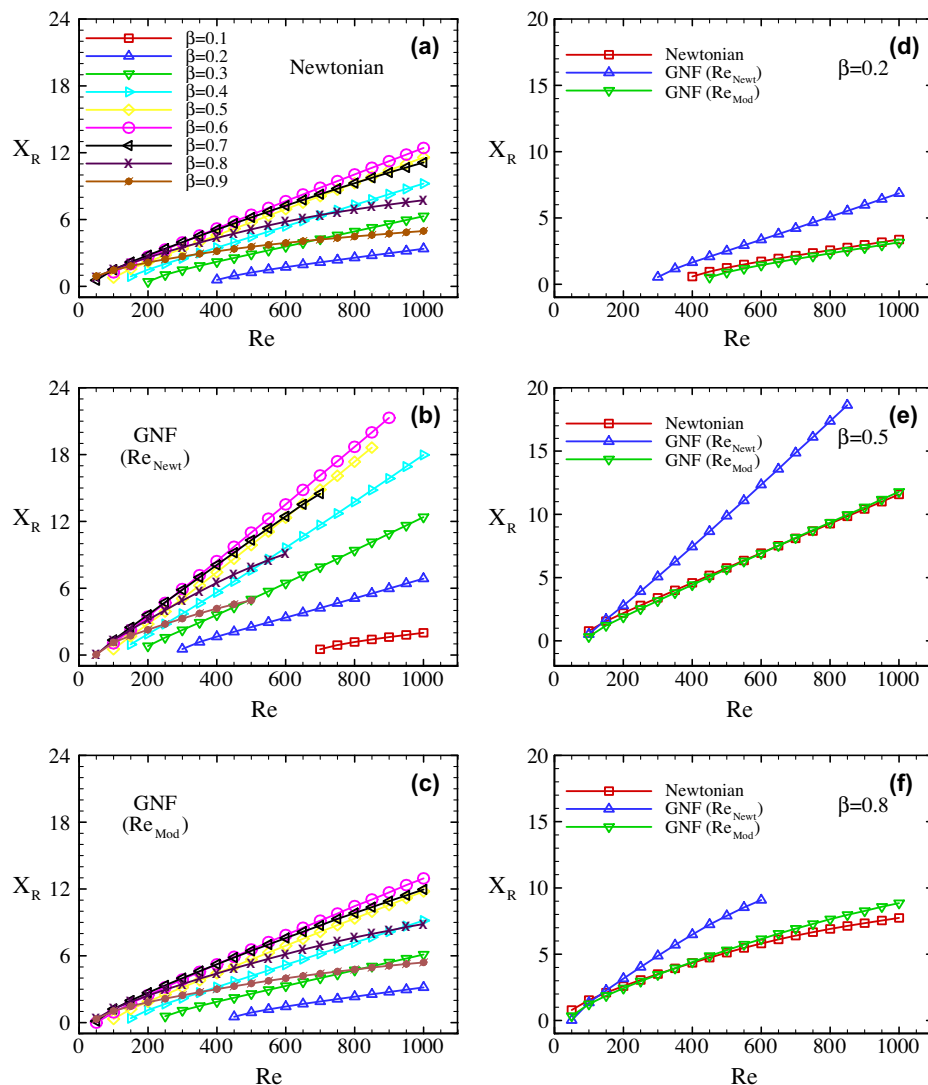


**Fig. 3.** Variation of the horizontal eddy size ( $X_R$ ) with inertia ( $Re$ ) and extraction ratio ( $\beta$ ), for Newtonian (a) and GNF fluids (b –  $Re_{Newt}$ ; c –  $Re_{Mod}$ ). Comparison for  $\beta = 0.2$  (d);  $0.5$  (e);  $0.8$  (f).

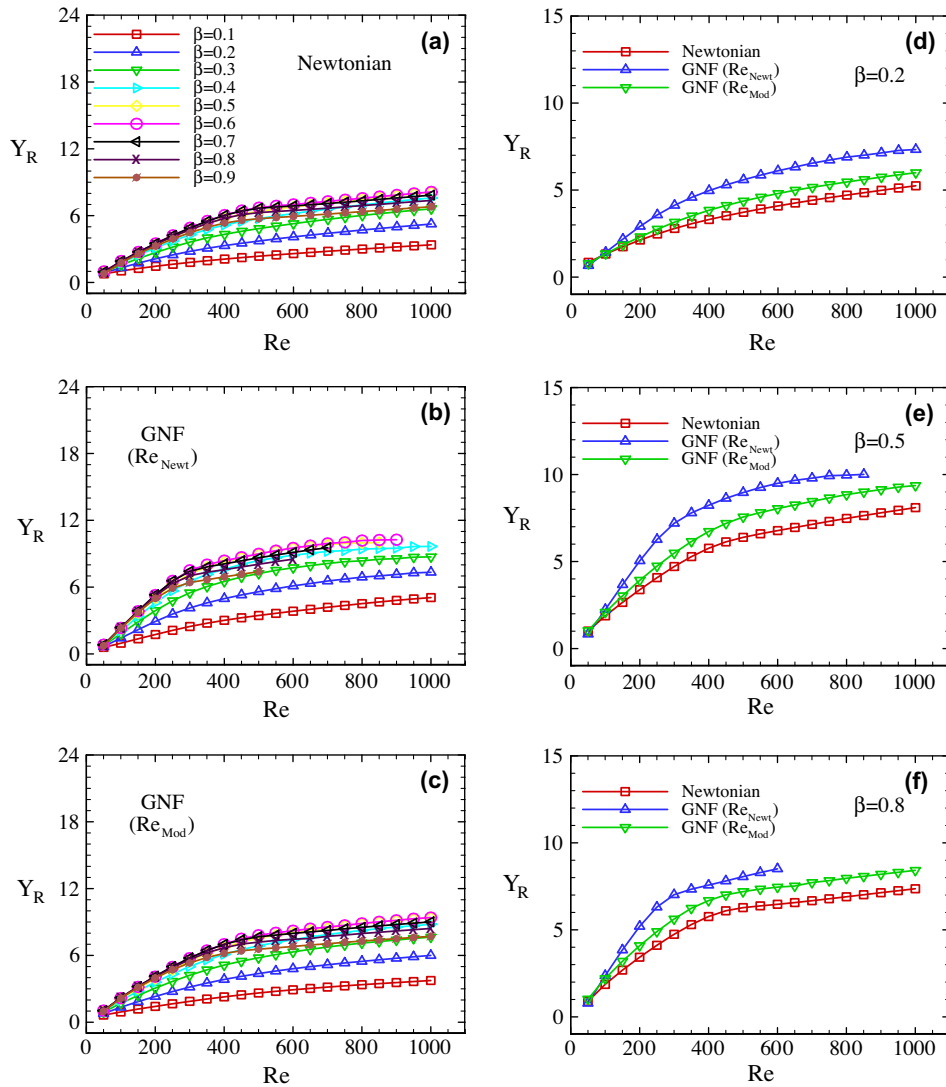


**Fig. 4.** Variation of the vertical eddy size ( $Y_R$ ) with inertia ( $Re$ ) and extraction ratio ( $\beta$ ), for Newtonian (a) and GNF fluids (b –  $Re_{Newt}$ ; c –  $Re_{Mod}$ ). Comparison for  $\beta = 0.2$  (d); 0.5 (e); 0.8 (f).

Reynolds number, when the Newtonian and non-Newtonian viscosity magnitudes become very different. This behaviour is easily explained as being caused by shear-thinning in viscosity; the parameters of the Carreau-Yasuda model for the GNF fluid were adjusted at the specific value of  $Re = 102$  and, for this low level of inertia, the predictions are very similar for the two fluids (Newtonian and GNF) independently of the  $Re$  definition. At higher velocities (increased  $Re$ ), the shear rate also increases and shear thinning becomes important, leading to a significant reduction of viscosity  $\eta$  ( $\eta < \eta_N$ ). Therefore the actual Reynolds number  $Re$  becomes much larger than the Newtonian Reynolds number based on a constant  $\eta_N$  viscosity, that is  $Re > Re_N$ . As a consequence, the calculations of the GNF flow with a  $Re_{Newt}$  effectively occur at a larger  $Re$  and the eddy lengths so predicted are necessarily highly exaggerated.

This problem is solved with the Modified Reynolds method to define  $Re$ . Fig. 3a–c, for the horizontal recirculation, shows that the results for Newtonian and GNF fluids become then very similar, thus demonstrating that the non-Newtonian shear thinning effect could be accounted for by inertia when the Reynolds number is obtained in a consistent way. On the other hand, some discrepancies are observed in the vertical recirculation, where the GNF fluid with

the Modified Reynolds method presents larger eddies when compared to corresponding Newtonian solutions. In this case the shear thinning introduced by the Carreau-Yasuda model induces in fact an increase in the length of the recirculation bubbles formed in the secondary branch, as result of a local viscosity decrease in response to the high values of shear rate around the recirculation. However this effect is excessively accentuated when the Reynolds number is based on the Newtonian viscosity, in agreement with the results for the horizontal recirculation.

We turn now attention to the analysis of the vortex activity, as measured by the intensity of the recirculations, or the quantity of fluid moving inside each of the recirculation bubbles. The evolution of this characteristic is analysed following the same graphical sequence used before for the recirculation length. Figs. 5 and 6 show the vortex strength of the horizontal ( $\psi_H$ ) and vertical ( $\psi_V$ ) recirculations, as a function of Reynolds number and extraction ratio, displaying in general an increase of vortex strength with inertia, for both recirculations. The values of  $\psi_H$  and  $\psi_V$  were calculated on the basis of the minimum and maximum streamfunction in the domain, normalized with the streamfunction at inlet,  $\psi_{int} = Q_1$ , namely:  $\psi_H = |\psi_{min}|/\psi_{int}$  and  $\psi_V = (\psi_{max}/\psi_{int}) - 1$ .



In the case of the horizontal recirculation (Fig. 5), the vortex strength increases smoothly with Reynolds number for low flow rate ratios; on the other hand, for high values of  $\beta$ , the vortex strength increases quickly with inertia as  $Re$  is initially raised, starting from  $Re = 50$ , and for high values of  $Re$  the variation is smoother or becomes almost constant. Contrary to the observed for the vortex size (cf. Fig. 3), the variation of vortex intensity with flow rate ratio always shows a monotonous behaviour,  $\psi_H$  increasing with  $\beta$ .

Fig. 6 shows the variation of vortex strength for the vertical recirculation. In this case, inertial effects lead to a rapid increase of vortex intensity at small Reynolds numbers, followed by a smooth out of the rate of increase of  $\psi_V$  at higher values of  $Re$ . The GNF fluid presents a second abrupt increase of vortex strength, which is clearly visible for Reynolds numbers between 450 and 500 when these are based on the “Newtonian Reynolds method” (which effectively corresponds to much higher  $Re$ ). By examining in detail the evolution of streamlines it was found that this abrupt increase of  $\psi_V$  is caused by a division of the main bubble, leading to the existence of two smaller eddies inside the extremity of that main bubble, as it is illustrated in Fig. 7 which shows flow streamlines for successive values of Reynolds numbers.

That phenomenon is related to the interaction of the main vortex in the vertical branch and a secondary vortex, formed

downstream of the first, when  $Re$  is sufficiently high. Once the vorticity of the second vortex becomes large, it drives the first and pulls its eye to the zone where the two are in closer contact. The result is more clearly visible for the GNF fluid with  $Re$  based on the Newtonian Reynolds method, however it also occurs for both the Newtonian fluid and the GNF fluid when  $Re$  is obtained with the Modified Reynolds method, but at higher Reynolds numbers; the example of Fig. 7, having  $\beta = 0.8$ , occurs at  $Re_{Mod} \approx 800$ .

The variation of vorticity in the vertical recirculation with flow rate ratio presents a monotonous behaviour, but the trend in this case depends on the magnitude of the Reynolds number. For low Reynolds numbers ( $Re \leq 150$  approximately) the vortex strength decreases with the increase of  $\beta$ , while for high Reynolds numbers the vortex strength increases with  $\beta$ .

Regarding the differences between the two fluids, illustrated in the graphs on the right of Figs. 5 and 6, the conclusion is that the vortex intensities are always smaller for the GNF fluid, compared to the Newtonian fluid, although the discrepancies are not that significant. Again the Newtonian Reynolds method leads to vorticity magnitudes that are either higher or lower than those for the Newtonian fluid, showing once more the need of expressing the Reynolds number in a consistent way.

We start now the analysis of the shear stress fields by comparing predictions for the Newtonian and the GNF fluids. Inertia is

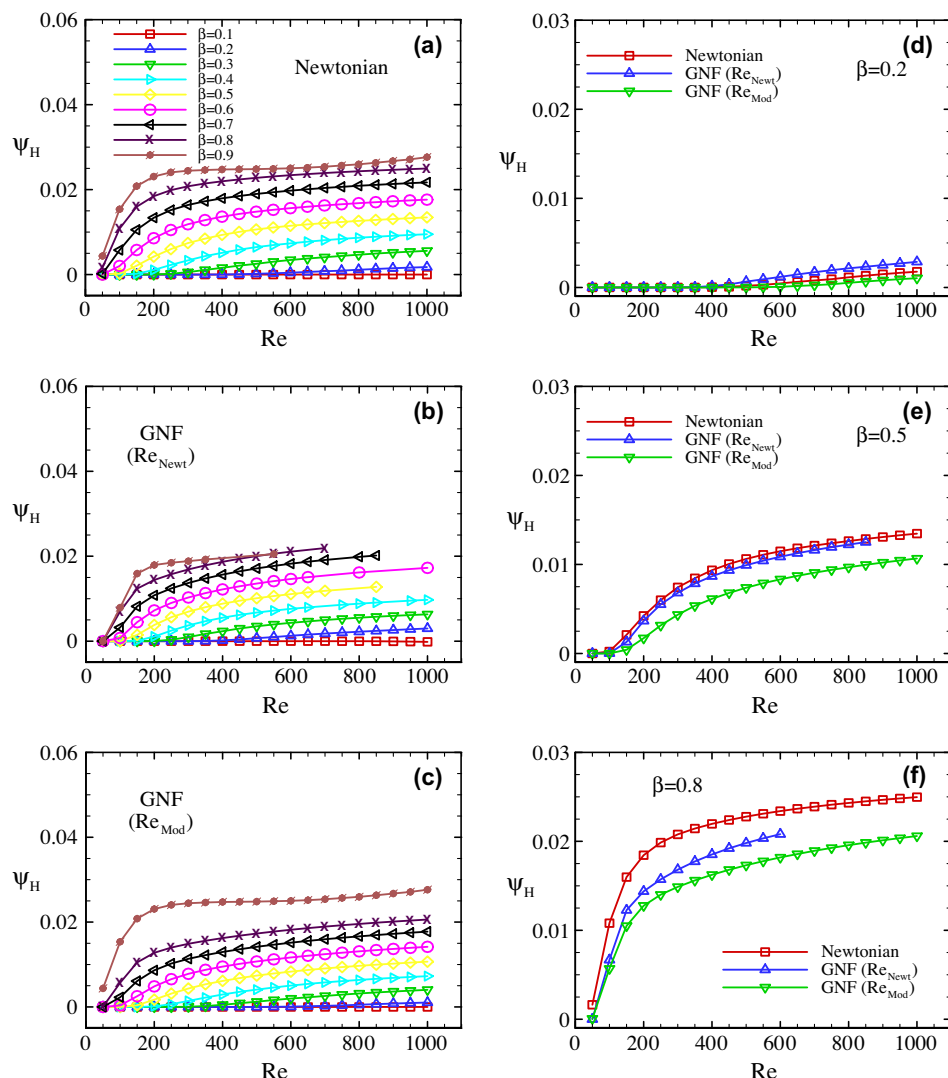
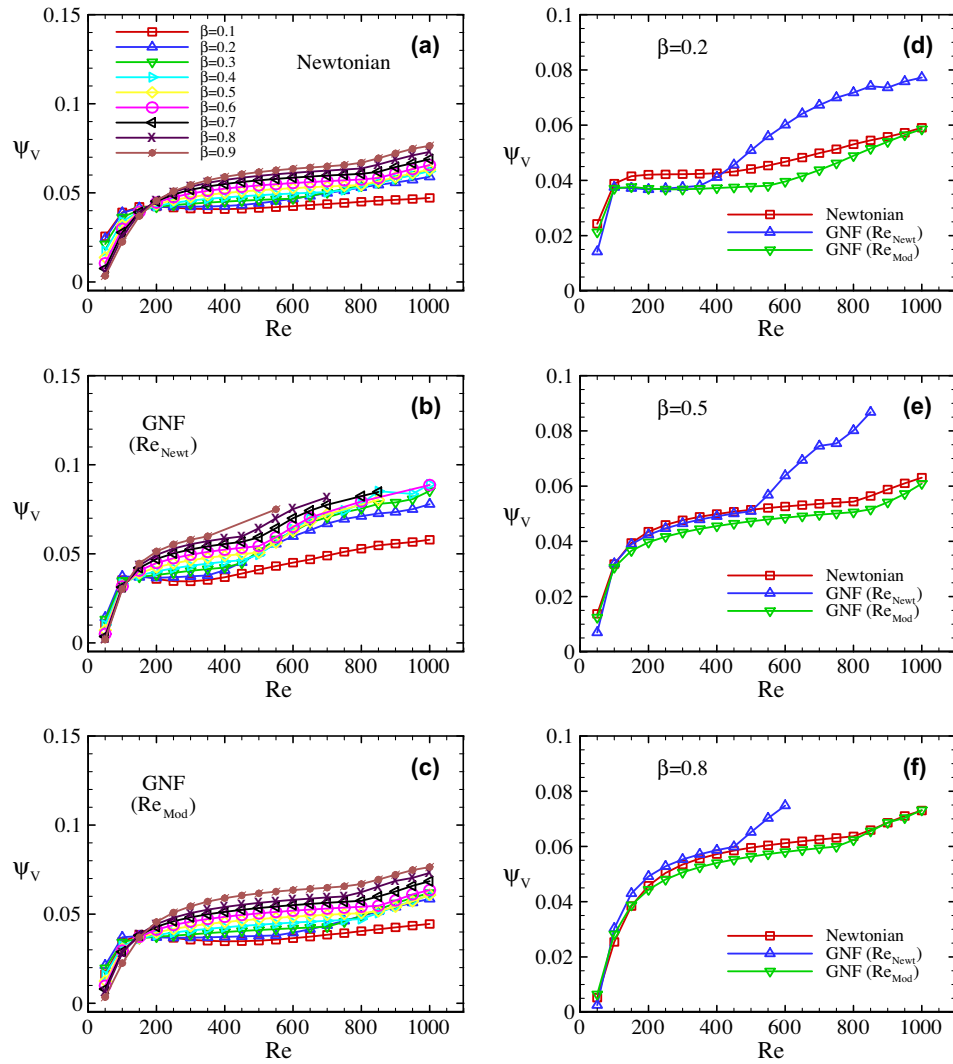


Fig. 5. Variation of the horizontal vortex intensity ( $\psi_H$ ) with inertia ( $Re$ ) and extraction ratio ( $\beta$ ), for Newtonian (a) and GNF fluids (b –  $Re_{Newt}$ ; c –  $Re_{Mod}$ ). Comparison for  $\beta = 0.2$  (d);  $0.5$  (e);  $0.8$  (f).



**Fig. 6.** Variation of the vertical vortex intensity ( $\psi_v$ ) with inertia ( $Re$ ) and extraction ratio ( $\beta$ ), for Newtonian (a) and GNF fluids (b –  $Re_{Newt}$ ; c –  $Re_{Mod}$ ). Comparison for  $\beta = 0.2$  (d); 0.5 (e); 0.8 (f).

characterised by a  $Re$  evaluated using the Modified Reynolds method. The study considers, separately, the influence of: (i) inertia, for constant flow rate ratio ( $\beta = 0.7$ ); (ii) flow rate ratio, for constant inertia ( $Re = 100$ ). All figures showing stress field contours also show the flow streamlines, in order to relate areas of recirculating flow with the shear stress magnitudes.

Figs. 8 and 9 present contour plots of the shear stress field ( $\tau_{xy}$ ) in the bifurcation zone for the Newtonian (Fig. 8) and the GNF fluids (Fig. 9), using four Reynolds numbers ( $Re = 100, 300, 500$  and  $700$ ) and the extraction ratio  $\beta = 0.7$ .

These figures show that, in general, there is an increase in the shear stresses as inertia is intensified, for both Newtonian and non-Newtonian fluid cases. The regions of maximum positive shear stress are located adjacent to the horizontal channel bottom wall and around the recirculation bubbles, following their frontiers along both the main channel and the side branch. In the secondary branch, areas of large  $\tau_{xy}$  occur downstream of the eddy, along the vertical wall upstream to the bifurcation.

The areas of minimum shear stresses become larger as the Reynolds number is increased, and are located close to the re-entrant corners and extend along the horizontal top wall, before the

bifurcation zone, and the downstream vertical wall, along the branch arm.

Fig. 10 shows the modulus of the shear stress field plot presented in Fig. 9, making it easier to observe the areas of very low shear stress close to the wall in the recirculation zones, while high stresses are generated in the recirculation boundaries, located in the main and the side branches. Such distribution induces high stress gradients and the possibility of shear stress oscillations, in space and time, which facilitate the inflammatory process and the triggering of an atherosclerotic plaque (Berger and Jou, 2000; Chien, 2008).

In general a comparison of the stress fields between the Newtonian and the GNF fluids shows only minor differences, with the Newtonian case presenting higher shear stresses (in modulus) when compared with GNF fluids. These discrepancies are quantified by maximum and minimum shear stress values given in Table 6, with data obtained from Figs. 8 and 9.

The influence of the extraction ratio upon the shear stress field can be inferred from Fig. 11 for the GNF fluid at a Modified Reynolds method of  $Re = 100$ . This figure shows a slight increase of maximum shear stress magnitudes (in modulus) with flow rate ratio; for low extraction ratios the higher shear stresses

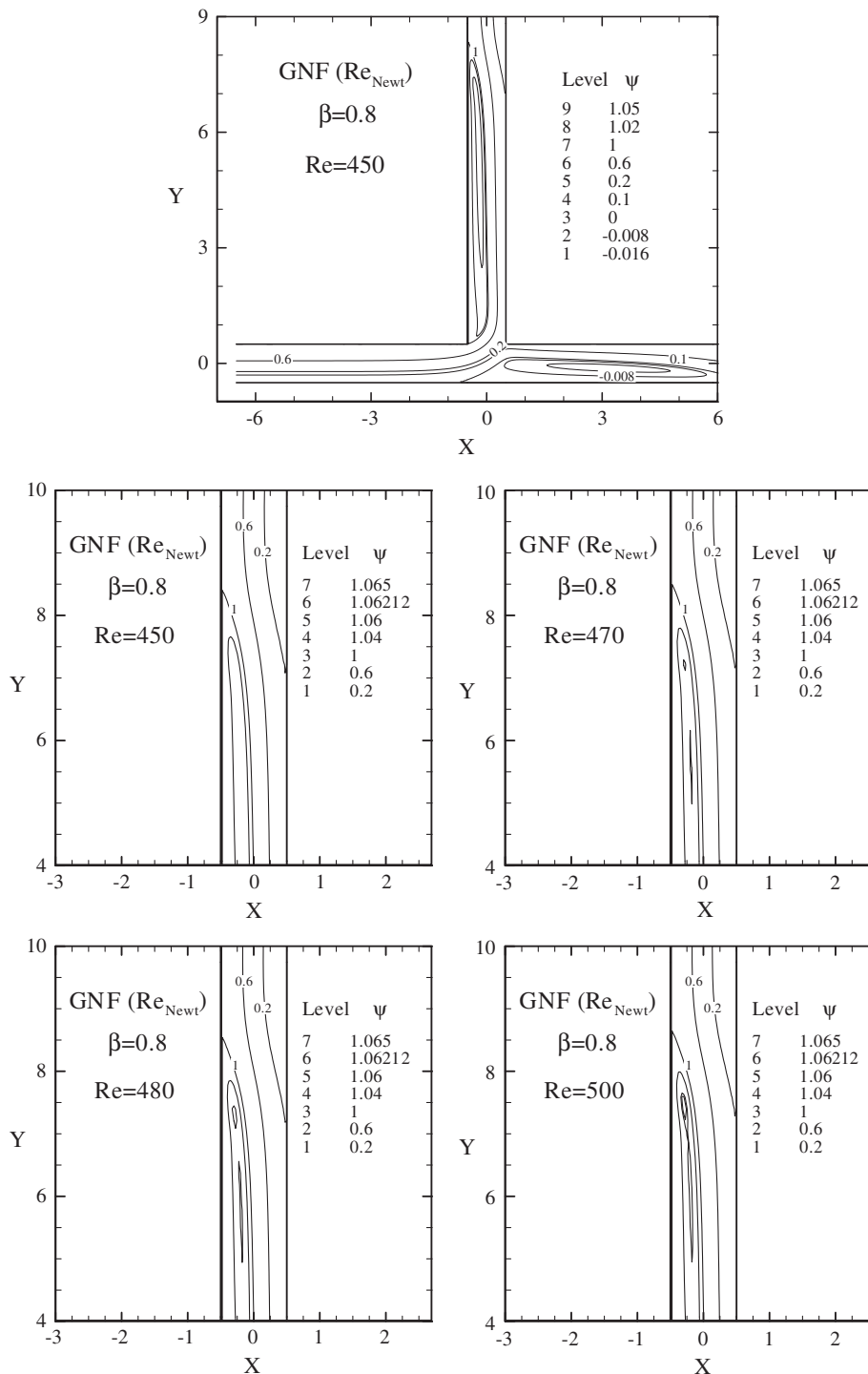


Fig. 7. Streamlines for the case  $\beta = 0.8$ ,  $Re_{Newt} = 450$ , with the GNF fluid, and details of the vertical vortex extremity as  $Re$  is increased.

are registered along the main duct in the wall layer, while for high extraction ratios they are registered along the secondary branch. In general, the maximum values of  $\tau_{xy}$  inside the flow domain occur in areas surrounding the eddy boundaries, which separate the inner recirculation bubbles and the outer main flow, and shear effects increase with the amount of fluid in these zones, thus justifying the displacement of maximum shear stresses from the main to the secondary branch with flow rate ratio increase.

### 5.1.2. Shear thinning variation

This section deals with the influence of shear thinning on the main flow characteristics near the junction zone. Shear thinning in viscosity was achieved by lowering the power law exponent ( $n$ ) of the Carreau-Yasuda model, from the limiting value  $n = 1$ , valid for the Newtonian case (no shear thinning), down to a low value  $n = 0.1$  (maximum shear thinning).

It is particularly important here, for a proper comparison of non-shear thinning with strong-shear thinning cases, to use a

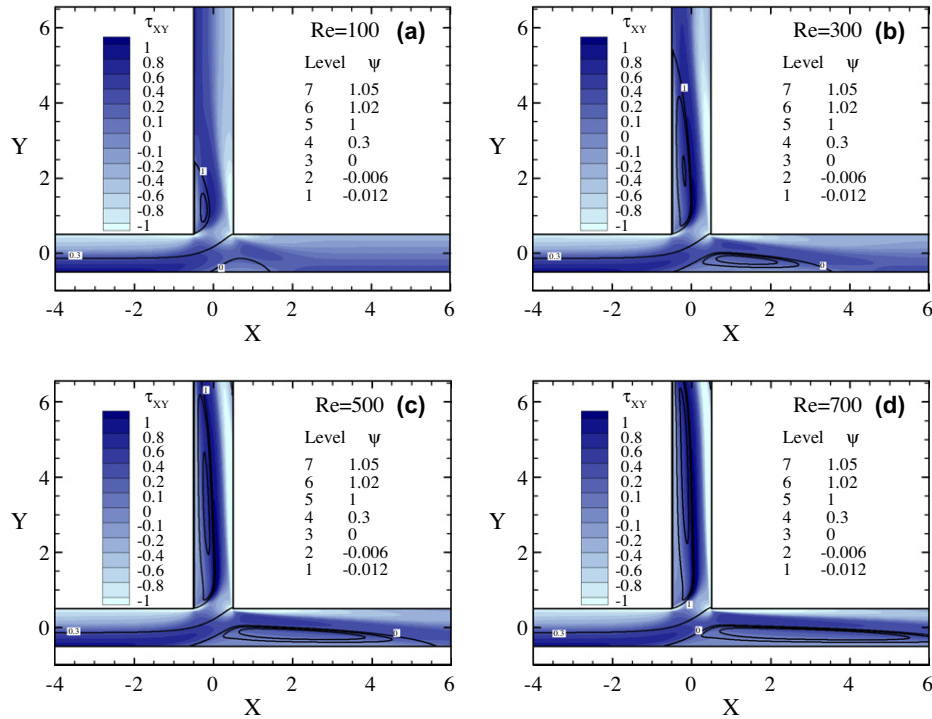


**Fig. 8.** Shear stress fields for increasing Reynolds numbers, at  $\beta = 0.7$ ; Newtonian cases: (a)  $Re = 100$ , (b)  $Re = 300$ , (c)  $Re = 500$  and (d)  $Re = 700$ .

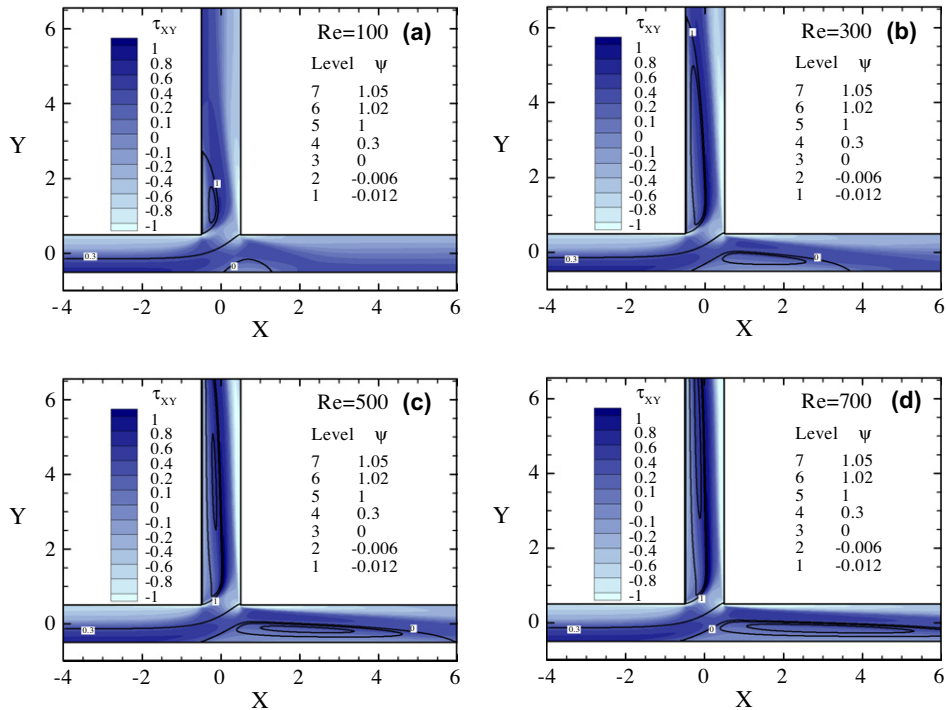


**Fig. 9.** Shear stress fields for increasing Reynolds numbers, at  $\beta = 0.7$ ; GNF case ( $Re_{Mod}$ ): (a)  $Re = 100$ , (b)  $Re = 300$ , (c)  $Re = 500$  and (d)  $Re = 700$ .

consistent Reynolds number definition. In this section the Reynolds number was based on the Modified Reynolds method, except the first results which serve precisely to show the inconsistency of using the Newtonian Reynolds method.

The results are discussed in two subsections: in the first, shear thinning is applied at constant flow rate ratio ( $\beta = 0.7$ ) and variable

Reynolds number; in the second, the flow rate ratio varies and the Reynolds number remains constant ( $Re = 102$ ).

**5.1.2.1. Shear thinning variation with constant flow rate ratio.** Fig. 12 presents the predicted results for the recirculation lengths as a function of Reynolds number and shear thinning, when the

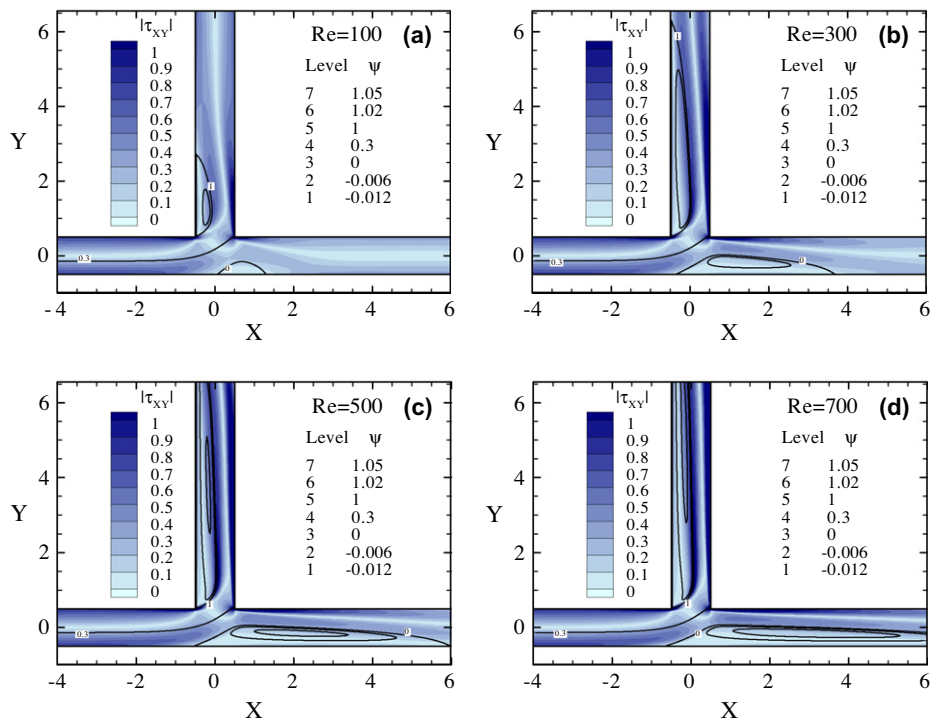


Fig. 10. Contours of shear stress modulus ( $|\tau_{xy}|$ ) for various  $Re$  at  $\beta = 0.7$  with the GNF fluid ( $Re_{Mod}$ ): (a)  $Re = 100$ , (b)  $Re = 300$ , (c)  $Re = 500$  and (d)  $Re = 700$ .

Table 6

Maximum and minimum shear stress for the Newtonian and GNF ( $Re_{Mod}$ ) fluids at various Reynolds numbers.

Fluid	Maximum shear stress ( $\tau_{XY_{Max}}/\tau_{w1}$ )		Minimum shear stress ( $\tau_{XY_{Min}}/\tau_{w1}$ )	
	Newtonian fluid	GNF fluid ( $Re_{Mod}$ )	Newtonian fluid	GNF fluid ( $Re_{Mod}$ )
$Re = 100$	0.99	0.76	-4.17	-2.95
$Re = 300$	1.12	0.96	-6.53	-4.99
$Re = 500$	1.35	1.16	-8.40	-6.62
$Re = 700$	1.53	1.32	-9.77	-7.85

Newtonian Reynolds method was used to define  $Re$ . There is clearly a large variation of the recirculation lengths for both vortices when  $n$  is varied, with a tendency for larger vortices when  $n$  is reduced and shear thinning sets in. However the Newtonian Reynolds method leads to a hidden variation of the actual Reynolds number and that explains the vortex length variation seen in Fig. 12. In fact when  $n$  is reduced at a constant inlet velocity  $\bar{u}_1$ , the shear rate increases and the actual viscosity diminishes, so the actual  $Re$  should in fact become larger. As a consequence, the vortex sizes tend to increase.

The graphs of Fig. 12 serve to demonstrate the need of expressing the Reynolds number in a consistent way when the viscosity is shear-thinning, such as in the Carreau-Yasuda model. The next results shall use the Modified Reynolds method and thus express the influence of shear thinning in the definition of Reynolds number, which should solve the problem of being in possession of a consistent  $Re$ .

Fig. 13 presents the same recirculation length data of Fig. 12 but this time  $Re$  is based on the Modified Reynolds method. The size of the recirculation bubbles still increases with inertia, for all shear thinning intensities (measured by  $n$ ), but the variability seen in Fig. 12 is now much reduced becoming clear that, when a proper

normalization of inertial effects is applied, the dimensions of the vortices formed by the bifurcating flow are little affected by shear-thinning. It is possible, however, to infer from Fig. 13 that the GNF fluids show higher recirculation lengths, although the shear thinning influence does not present a monotone behaviour. Initially the recirculation lengths increase with power law exponent up to a maximum for  $n \approx 0.6$  in this particular case ( $\beta = 0.7$ ), followed by a decrease to the minimum vortex size which is obtained for the Newtonian case, with  $n = 1$ . This tendency is more clear at high  $Re$ . We may thus conclude that the normalization inherent to the Modified Reynolds method does not imply a perfect match of the Newtonian and the corresponding non-Newtonian flow cases. This could be expected since that normalization is based on a global characteristic shear rate and does not account for the local details of the flow and the variations of  $\dot{\gamma}$ . Therefore an influence of shear-thinning remains in the results of Fig. 13b (and Fig. 16b below), with the larger variation occurring in the middle range of the power law exponent  $n \approx 0.5 - 0.6$ . Such feature may be explained by noticing that as  $n \rightarrow 1$  we recover the Newtonian case with  $\eta \rightarrow \eta_0$ , and with  $n \rightarrow 0$  the viscosity decays quickly and for most  $\dot{\gamma}$  it remains constant at  $\eta \rightarrow \eta_\infty$  (and the flow behaviour is again Newtonian-like).

The amount of fluid recirculating inside each of the horizontal and vertical eddies, or vortex strength, is presented in Fig. 14. The influence of shear thinning on both eddy intensities is again quite small, provided the  $Re$  is defined in a consistent way (Modified Reynolds method), and the behaviour is the contrary of that observed for the eddy size. This is easily understood: the higher vorticities are always obtained for the Newtonian case with  $n = 1$  since the viscosity is then more pronounced and the recirculating vortex is thus proner to drag more fluid, enhancing its intensity. So, both  $\psi_H$  (horizontal eddy intensity) and  $\psi_V$  (vertical eddy intensity) diminish as the power law index is reduced from  $n = 1$ , albeit the effect being small.

Fig. 15 displays the influence of shear thinning on the shear stress field, for four different power law exponents, at a Reynolds



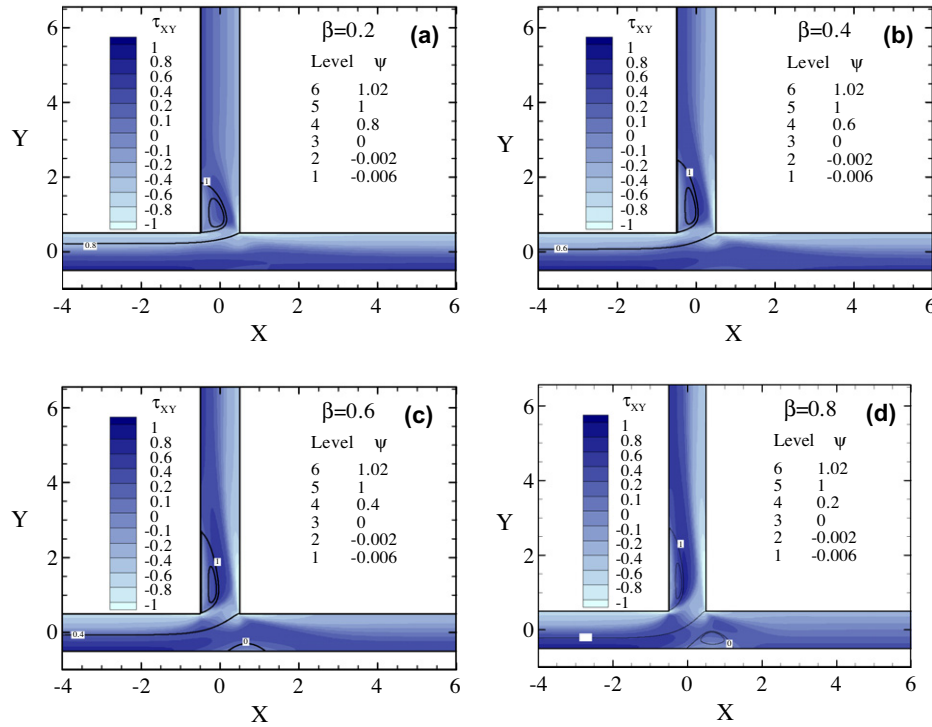


Fig. 11. Variation of the shear stress field ( $\tau_{xy}$ ) with extraction ratio  $\beta$  for  $Re_{Mod} = 100$ : (a)  $\beta = 0.2$ , (b)  $\beta = 0.4$ , (c)  $\beta = 0.6$  and (d)  $\beta = 0.8$ .

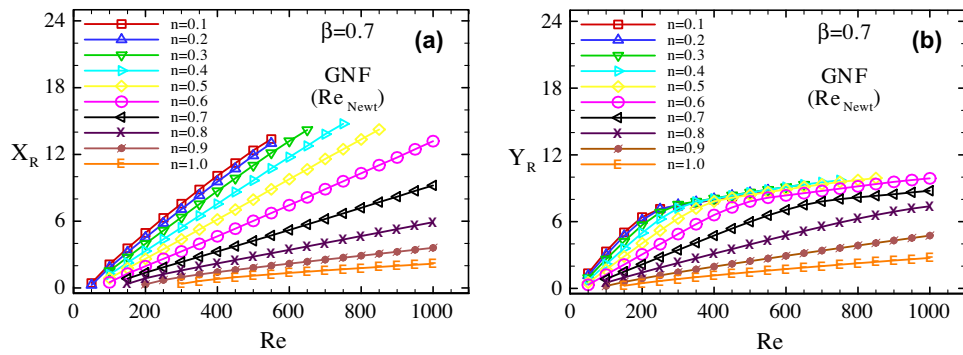


Fig. 12. Variation of  $X_R$  (a) and  $Y_R$  (b) with shear thinning and  $Re$  for GNF fluids with Newtonian Reynolds method and  $\beta = 0.7$ .

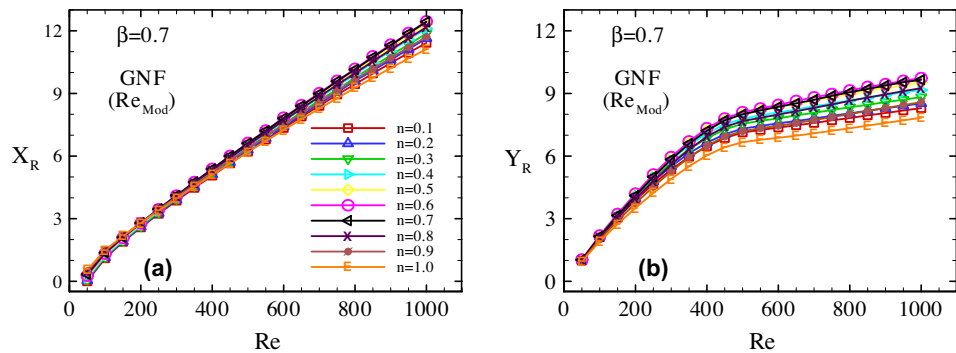


Fig. 13. Variation of the horizontal  $X_R$  (a) and vertical  $Y_R$  (b) eddy sizes with shear thinning and inertia ( $Re$  based on Modified Reynolds method), at  $\beta = 0.7$ .

number of  $Re = 500$  and an extraction ratio of  $\beta = 0.7$ . The shear stress fields for all the power law exponents presents a similar behaviour to the case with  $n = 0.3568$  analysed before. Hence, we

way conclude that shear thinning, provided  $Re$  is defined consistently, does not influence significantly the shear stress field. The resulting variations on  $\tau_{xy}$  are not monotonous with  $n$ ; when  $n$  is

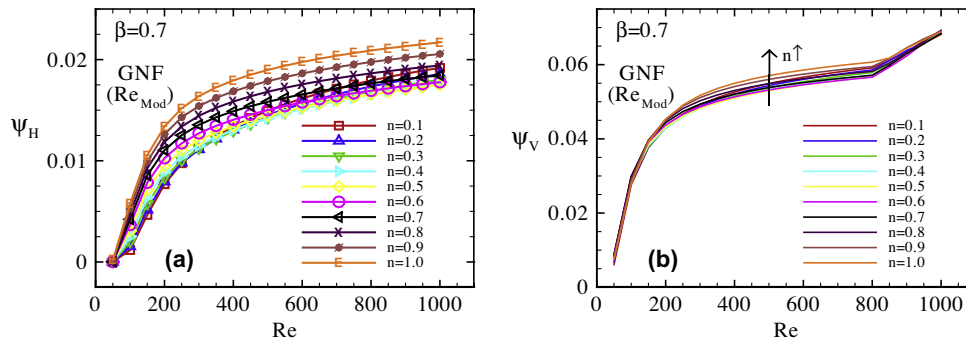


Fig. 14. Variation of the horizontal  $\psi_H$  (a) and vertical  $\psi_V$  (b) eddy intensities with shear thinning and inertia ( $Re$  based on Modified Reynolds method), at  $\beta = 0.7$ .

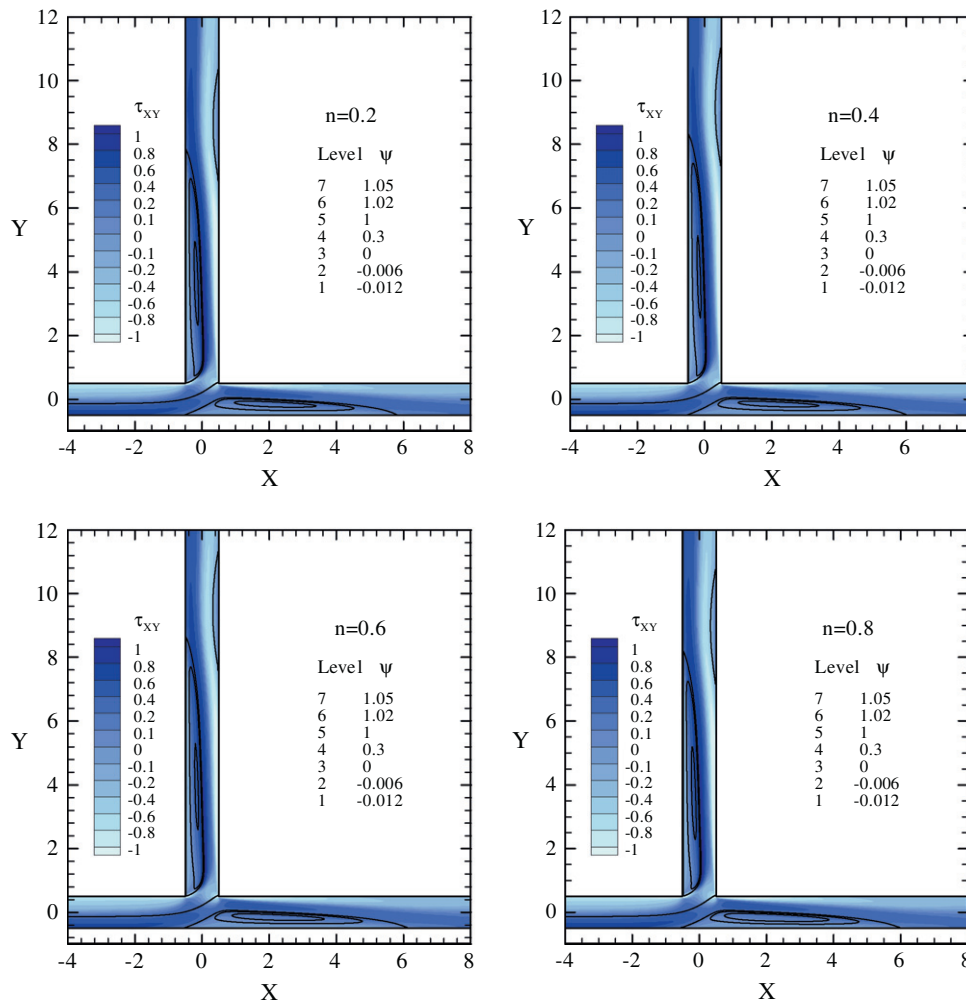


Fig. 15. Variation of the shear stress field ( $\tau_{XY}$ ) with  $n$ , for the GNF fluid, at  $\beta = 0.7$  and  $Re_{Mod} = 500$ .

raised from  $n = 0.1$ , there is first a decrease in modulus of  $\tau_{XY}$  and, for  $n > 0.6$ ,  $\tau_{XY}$  increases up to a maximum attained for the Newtonian case, with  $n = 1$ . The maximum and minimum values of shear stress, for the several shear thinning intensities here considered, are compiled in Table 7.

**5.1.2.2. Shear thinning variation with constant inertia.** The present subsection focuses on the influence of shear thinning upon the bifurcation flow pattern for different flow rate ratios, keeping the Reynolds number constant and equal to 102. Fig. 16 illustrates

the variation of the two recirculation lengths with flow rate ratio and shear thinning. The effect of flow rate ratio is similar to what was observed in previous results at constant shear thinning: there is an increase of eddy size up to a maximum, when  $\beta \approx 0.7$ , followed by a decrease after that. In this particular case (low  $Re = 102$ ) the value of flow rate ratio for which the recirculation lengths attain their maximum magnitudes is slightly different from the obtained earlier, which was  $\beta = 0.6$ . The left figure (Fig. 16a), giving the horizontal recirculation length, only shows results for extraction ratios higher than 0.5 because for lower  $\beta$  there is no

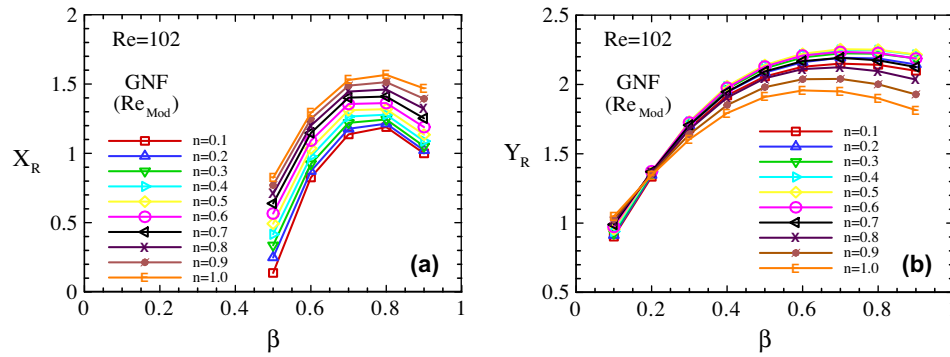


Fig. 16. Variation of the horizontal  $X_R$  (a) and vertical  $Y_R$  (b) eddy sizes with shear thinning and extraction ratio  $\beta$ , for GNF fluids at  $Re_{Mod} = 102$ .

Table 7

Maximum and minimum shear stress for a GNF fluid as a function of power law exponent, at  $\beta = 0.7$  and  $Re_{Mod} = 500$ .

Power law index	$n = 0.1$	$n = 0.2$	$n = 0.3$	$n = 0.4$	$n = 0.5$	$n = 0.6$	$n = 0.7$	$n = 0.8$	$n = 0.9$	$n = 1.0$
Maximum shear stress ( $\tau_{XY_{Max}}/\tau_{w1}$ )	1.25	1.22	1.19	1.15	1.12	1.11	1.13	1.18	1.26	1.35
Minimum shear stress ( $\tau_{XY_{Min}}/\tau_{w1}$ )	-7.57	-7.25	-6.86	-6.44	-6.04	-5.76	-5.77	-6.20	-7.10	-8.40

horizontal bubble at this Reynolds number ( $Re = 102$ ); for higher values of  $Re$  the horizontal recirculation is formed even for small flow rate ratios, as shown before in Fig. 3.

For the Reynolds number used in Fig. 16 the horizontal recirculation length presents a monotone variation with shear thinning, increasing with the power-law index  $n$  up to a maximum for the Newtonian case with  $n = 1$ .

In the secondary branch, the effect of shear thinning on the recirculation length is only appreciable at high extraction ratios. For low flow rate ratios ( $\beta \leq 0.2$ ) the influence of shear thinning is negligible, while for higher values of  $\beta$  the behaviour is not monotonic:  $Y_R$  increases to maximum values when  $n$  is raised from  $n = 0.1$  up to  $n = 0.5$ , and the vortex size decreases after that, down to minimum values for the Newtonian case. An explanation for this trend was given above, when discussing Fig. 13b.

## 5.2. Non-Newtonian inelastic unsteady flows

This section deals with unsteady periodic flows of the same Carreau-Yasuda GNF fluid of the previous section and, after a general introduction and a check on the numerical accuracy (Section 5.2.1), the main results are discussed in two subsections: (Section 5.2.2) shear thinning effects at constant inertia and flow rate ratio, and (Section 5.2.3) flow rate ratio effects at constant inertia and shear thinning.

For these unsteady flows a pulsatile velocity profile is imposed at the inlet, corresponding to the theoretical solution valid for Newtonian fluids generated by the sinusoidal pressure gradient of Eq. (8). Khodadadi et al. (1988) and Miranda et al. (2008) have employed the same time-dependent inlet conditions in their T-junction flow studies. After an initial transient regime which is of no interest here, the flow reaches a well-established periodic regime in which the main flow characteristics (such as vortex patterns) change over a cycle, and peculiar flow phenomena may also occur which are absent in the corresponding steady case.

Fig. 17 illustrates the flow development over one cycle by means of streamlines superimposed onto shear stress field contours, so that it is possible to correlate the two. For this example the GNF fluid possesses the characteristics given in Table 1, the Reynolds number was constant ( $Re = 102$ ) and also the flow rate ratio ( $\beta = 0.7$ ); the time step employed was 0.005, which is sufficiently low to ensure adequate time accuracy (tests are presented below).

From this figure it is possible to observe that both eddies evolve during the cycle, changing in shape and size, which grows and eventually diminishes at the end of the cycle period, with the eddies detaching and being carried along by the flow. These features create a wave-like streamline behaviour which is more visible in the side branch flow, where the main eddy is not completely removed. Once more, high shear stress layers tend to be formed along the recirculation boundaries and on the re-entrant corners, while small values are registered inside the recirculating eddies. Since these change over the cycle, the shear stress accompany that evolution, with their magnitudes tending to increase (in modulus) up to a maximum near 25% of the cycle ( $\omega t \approx 90^\circ$ ), decreasing after that to the minimum values at approximately 75% of the cycle ( $\omega t \approx 270^\circ$ ), and increasing again by the end of the cycle. Another consequence of the recirculation length variation over the cycle is that certain points of the T-junction walls can fall either inside or outside the recirculations and thus experience very different shear stress magnitudes during the cycle development, therefore increasing the probability of inflammation at these points on the wall, as described before.

It is noted that the vortex in the secondary branch is present during the whole cycle (Fig. 17), while the horizontal recirculation in the main branch is only present in part of the cycle, being formed after the cycle starts and disappearing before it ends.

Fig. 18 displays the evolution of the points of separation and reattachment of both eddies, and their lengths, during the pulsating cycle. Both recirculations increase during the cycle to maximum values that occur at about 60% of the cycle duration and decrease after that (Fig. 18b). The horizontal recirculation length varies as a consequence of the movement of both the separation ( $X_s$ ) and the reattachment ( $X_r$ ) points, while the length of the vertical recirculation depends only on the movement of the reattachment point ( $Y_r$ ), since the point of separation ( $Y_s$ ) is defined by the geometry and remains unchanged during the cycle (Fig. 18a).

Fig. 18 reveals a phenomenon already reported in the previous work with Newtonian fluids (Miranda et al., 2008). There is an abrupt reduction in the length of the vertical recirculation after about 3/4 of the cycle are completed, as shown in more detail in Fig. 19 for  $0.75 \leq t \leq 0.875$ . This occurrence is associated with the breakup of the main recirculation into two vortices due to the emergence of a new bubble near the wall, as seen through the sequence of plots in Fig. 19 for intermediate values of time, between 0.75 and 0.875. In Fig. 18a the red line (square symbols) cor-

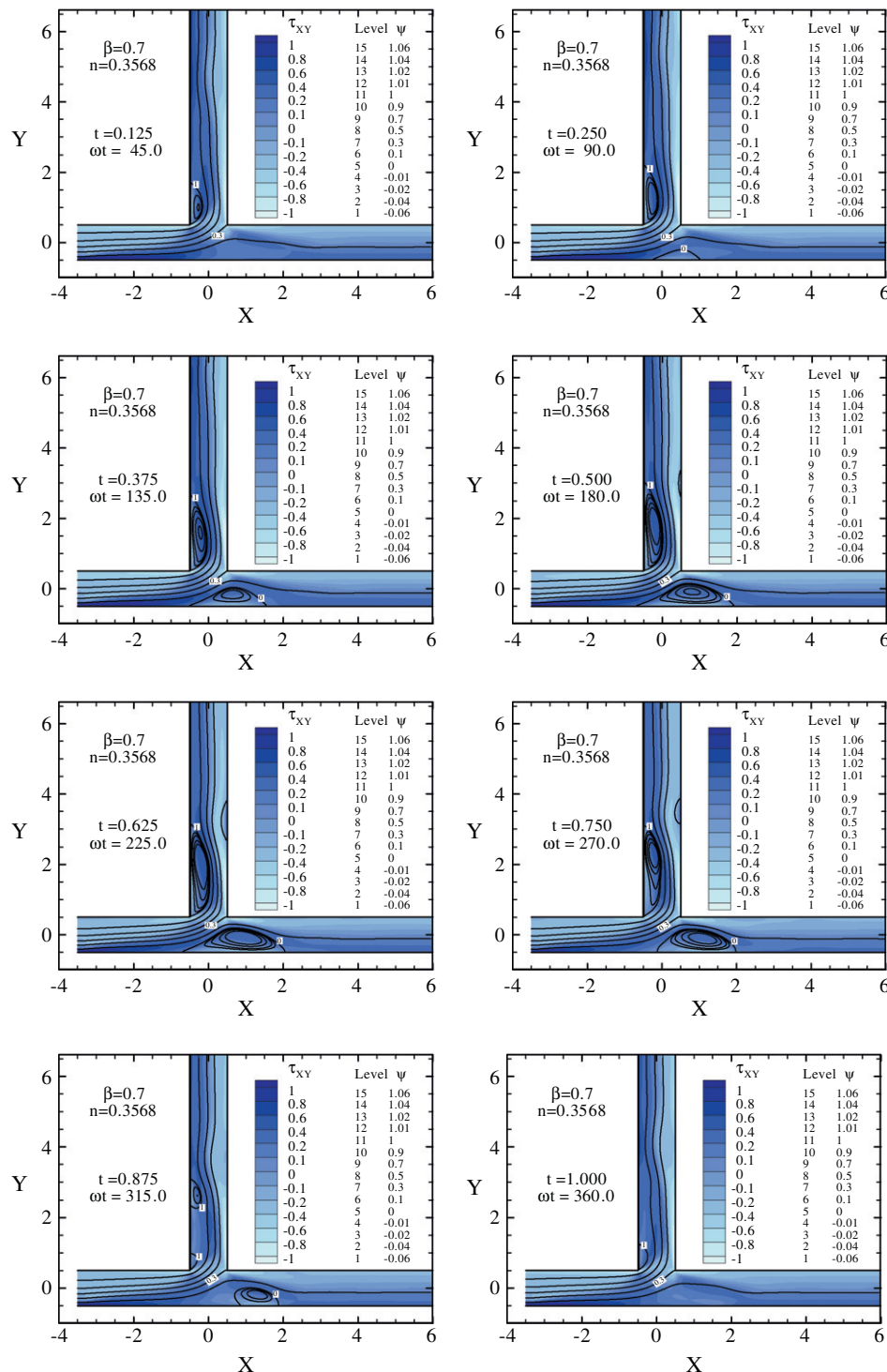


Fig. 17. Streamlines and shear stress fields over a cycle ( $\beta = 0.7$ ;  $n = 0.3568$  and  $\Delta t = 0.005$ ).

responds to the first reattachment point (unique before the division) and the purple line (circular symbols) to the second reattachment point associated with the second recirculation created after bubble division, which eventually disappears later in the cycle when  $t \geq 0.9$  (Figs. 17 and 19).

The vertical bubble size  $Y_R = Y_{R1}$  in Fig. 18b corresponds to the length of the single bubble, before the bubble separation phenomenon just described occurs, and, after that, to the bubble closer to the junction corner, while the size of the other recirculation bubble resulting from the breakup of the main bubble is denoted as  $Y_{R2}$  in the figure.

Note that the breakup of the vertical eddy illustrated in Fig. 19 is associated with flow unsteadiness (generated by the periodic pressure gradient imposed at inlet) and has no relation to the two small eddies of Fig. 7, which appear as  $Re$  is increased in steady flow.

### 5.2.1. Accuracy tests

Two types of accuracy tests are required for time-dependent periodic flows, such as the ones analysed here. There is the need to establish that the time discretisation error is small, and that there is repetition of the solution for consecutive periods.

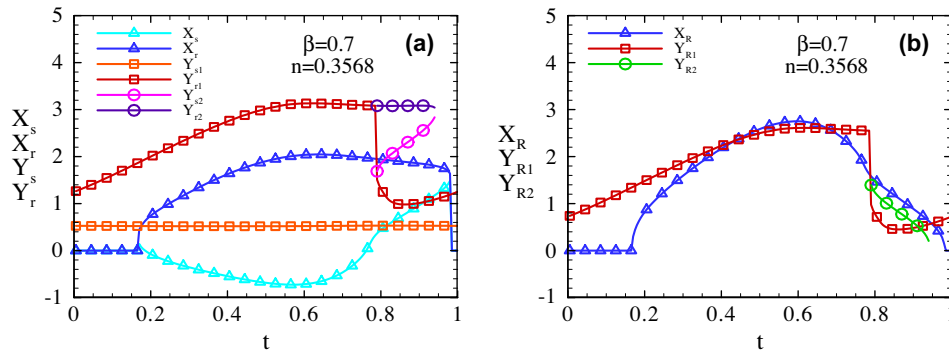


Fig. 18. Variation with time of the separation and reattachment points (a) and the recirculation lengths (b) ( $\beta = 0.7$ ;  $n = 0.3568$  and  $\Delta t = 0.005$ ).

For unsteady flow simulations, the time step needs to be sufficiently small so that it guarantees a solution that is independent of that same time step value. In these circumstances we have adopted the same time step used by Miranda et al. (2008), since the flows are similar and the geometry is identical. The base or reference time step is denoted  $\Delta t_2 = 0.005$  (in nondimensional terms) dividing the sinusoidal cycle into 200 time advances.

The suitability of such base time step value was verified by simulations using three consecutively refined time steps. The coarser time step is obtained by doubling the reference time step (thus  $\Delta t_1 = 0.01$ ) and the more refined by halving that step (thus  $\Delta t_3 = 0.0025$ ), with the temporal resolution being improved with 400 time advances to represent a whole cycle.

As a choice for the solution functional used in the accuracy tests, we take the recirculation length evolution during one cycle, which is given for different time steps in Fig. 20. These two graphs, for the sizes of the horizontal and vertical recirculation lengths at  $Re = 102$  and  $\beta = 0.7$ , for the base GNF fluid ( $n = 0.3568$ ), show a perfect agreement between the numerical results corresponding to the three time step values mentioned above, with only minor differences visible when the separation of the vertical recirculation occurs. These results demonstrate adequate time resolution and that the discretisation error is ultimately controlled by the spatial discretisation (here the mesh was M2 of Table 2) and not by the time discretisation.

However in order to verify with more detail the agreement of results for the three time steps, Fig. 21 shows the evolution during one period of the percentage relative difference between the eddy size solutions with the smallest and the intermediate time steps (designated  $\Delta t_{3-2}$ ) and the difference between the smallest and the largest time steps (designated  $\Delta t_{3-1}$ ).

The differences are very small in almost the entire cycle ( $\Delta\phi \leq 0.1$ , Fig. 21a), except the time instants when the horizontal recirculation is formed and disappears and when the vertical recirculation collapses into two smaller eddies. At these instants the variation in time of the solution is sharp, with the time derivative of  $X_R$  and  $Y_R$  becoming virtually infinite, and therefore amplifying any small difference between the various time discretisations (the peaks observed in Fig. 21b). However, even at these particular time instants the differences between solutions obtained with the smallest and the reference time steps ( $\Delta t_{3-2}$ ) are acceptable, registering variations smaller than 8%, thus demonstrating the adequate temporal resolution obtained with the intermediate time step ( $\Delta t_2$ ) adopted as reference  $\Delta t$ .

Fig. 22 shows the repetition checks which are useful, in particular, to evaluate the minimum number of cycles required to obtain identical solutions at consecutive cycles, thus guaranteeing a truly periodic solution. The present accuracy test compares the recircu-

lation lengths and several pointwise solution values, located in the middle of the main channel ( $Y = 0$  and  $X = 12.5$ ), over 40 consecutive cycles.

The local variables shown in Fig. 22c and d are the shear stress and the vertical velocity component, which have the advantage of attaining very low values along the centre line in the main channel (theoretically  $\tau_{xy} = 0$  and  $V = 0$  at  $Y = 0$  under fully developed conditions) and so, the fine scale in the figure tends to magnify any small differences between values for the various cycles. It is seen that approximately 7 cycles are necessary to obtain identical solutions between consecutive cycles when one looks to the  $V_1$  velocity component, while the recirculation lengths (Fig. 22a and b) are similar after only two cycles thus being a rather imprecise variable to assess cyclic repetition. For reasons of being on the safe side, all results presented were calculated after an initial transient of 40 cycles to ensure identical solutions between consecutive cycles (cycles 40 and 41) for all quantities.

### 5.2.2. Influence of shear thinning at constant inertia and flow rate ratio

The influence of shear thinning was tested at constant inertia ( $Re = 102$ ) and flow rate ratio ( $\beta = 0.7$ ). When  $n$  is varied,  $Re = 102$  is kept constant by basing its calculation on the Modified Reynolds method. The mean velocity at inlet is maintained unaltered and the effective viscosity identical to the Newtonian case by adjusting the value of the zero shear rate viscosity ( $\eta_0$ ) in the Carreau-Yasuda model. The following figures show the influence of shear thinning on the recirculation lengths. It is instructive first to see how the recirculation lengths change when  $n$  is varied without being careful in maintaining the same level of inertia, that is, with the Newtonian Reynolds method.

This is shown in Fig. 23 where, once again, large variations of recirculation lengths are observed for the various power law exponents  $n$ , with a tendency for much larger recirculations as  $n$  is decreased, as a consequence of higher effective Reynolds number (on account of shear thinning), and with inconsistent results for the case with  $n = 1$  (orange line with hollow symbols) which do not match the Newtonian base case (orange line with filled square symbols).

Obviously the Newtonian solution is close to the GNF solution for  $n = 0.4$  because the viscosity was adjusted for that situation (the base case). When the Reynolds number is expressed in a consistent way, the first immediate consequence is that equal solutions result for the Newtonian and the GNF fluid with  $n = 1$ .

Besides, as shown in Fig. 24, very little changes in magnitudes of  $X_R$  and  $Y_R$  are observed as  $n$  is varied, when compared with results of Fig. 23. In general, close inspection reveals that an increase in shear thinning (decrease of  $n$ ) results in a slight increase of the recirculation lengths. For the horizontal recirculation, shear thinning also results in shorter residence times over the cycle, while



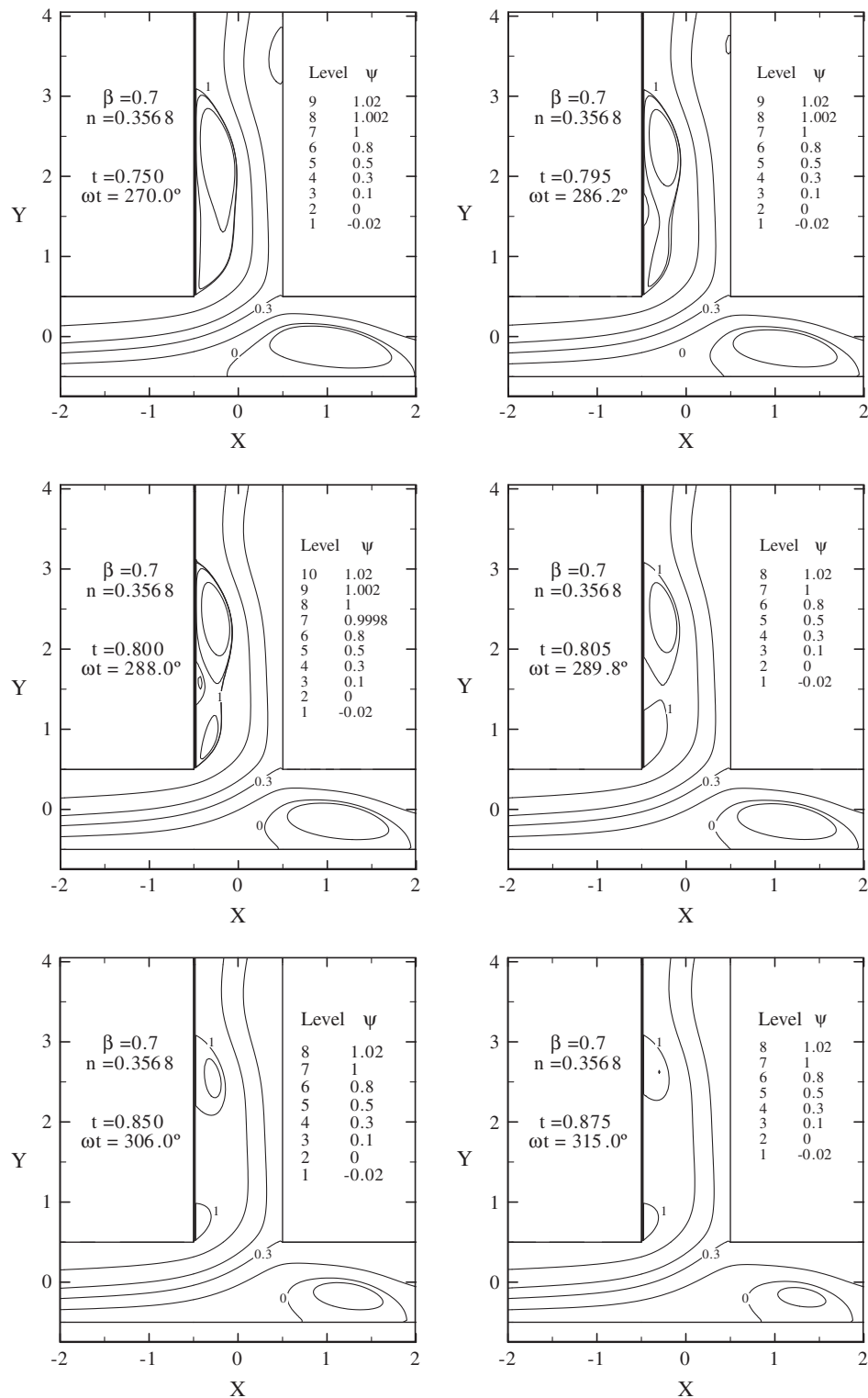


Fig. 19. Detail of the subdivision of the vertical recirculation ( $\beta = 0.7$ ;  $n = 0.3568$  and  $\Delta t = 0.005$ ).

the vertical recirculation tends to split somewhat earlier (at  $t = 0.79$  when  $n = 0.1$ , and  $t = 0.815$  when  $n = 0.9$ ).

The next figure (Fig. 25) shows the vortex intensities during the cycle as  $n$  is varied. There is a monotone behaviour, showing eddy intensification with shear thinning, which is more pronounced in the vertical recirculation. With shear thinning, increased shear rates along the outside boundaries of the recirculations lead to

smaller viscosities and thus higher amount of fluid being driven into those recirculations, which result in the observed vortex intensity increase.

Additionally, the intensity of both recirculations increases during the development of the cycle to a maximum that occurs when it reaches about 60% of the period, and decreases after that. This is correlated with the variation of the recirculation lengths which

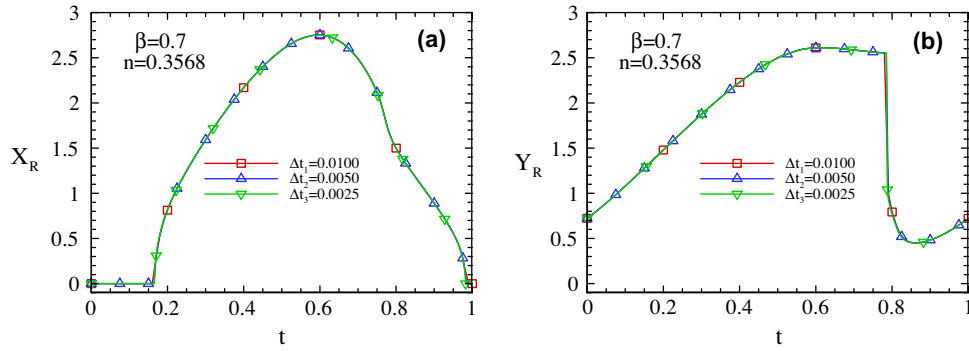


Fig. 20. Convergence of the predicted recirculation lengths ( $X_R$  (a) and  $Y_R$  (b)) with the time step size ( $\beta = 0.7$  and  $n = 0.3568$ ).

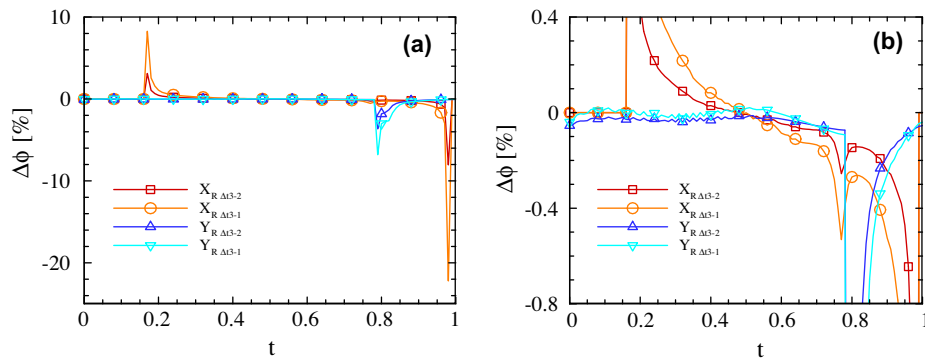


Fig. 21. Percentage difference between solutions for  $X_R$  and  $Y_R$  with time steps  $\Delta t_3$  and  $\Delta t_2$  (denoted  $\Delta t_{3-2}$ ) and  $\Delta t_3$  and  $\Delta t_1$  (denoted  $\Delta t_{3-1}$ ), with  $\Delta t_3 < \Delta t_2 < \Delta t_1$ . (a) Cyclic variation and (b) zoomed view.

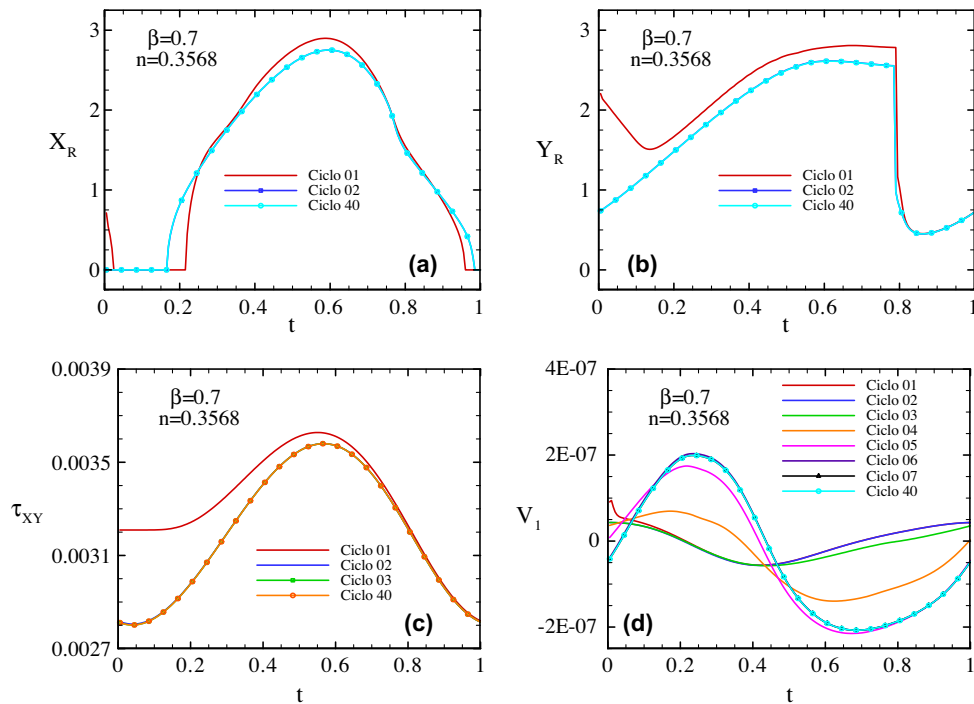


Fig. 22. Repetition over 40 cycles: recirculation lengths ( $X_R$  (a) and  $Y_R$  (b)) and pointwise shear stress (c) and vertical velocity component (d), at  $Y = 0$  and  $X = 12.5$ .

also increase up to a maximum for the same cycle interval and decrease subsequently. A quantification of such behaviour is given in Fig. 26 which plots the maximum eddy sizes and intensities, in the

cycle, as a function of  $n$ . Except for the side-branch eddy size, the variations are almost linear with  $n$ , with an increasing tendency as  $n$  decreases. It is therefore possible to conclude unambiguously

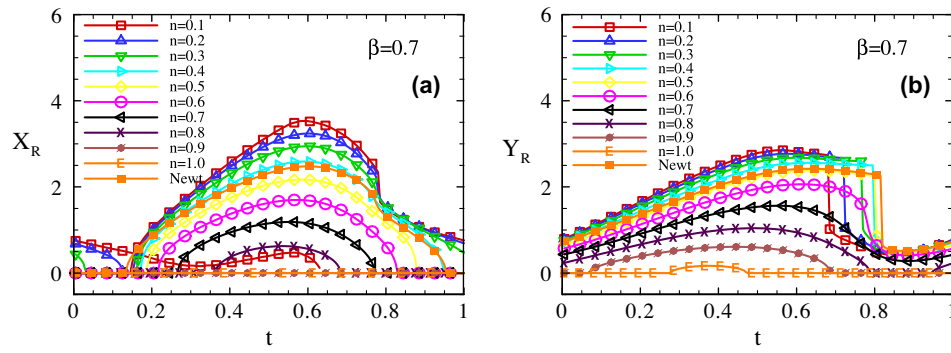


Fig. 23. Influence of shear thinning with the Newtonian Reynolds method: variation of vortex sizes  $X_R$  (a) and  $Y_R$  (b) with  $n$ .

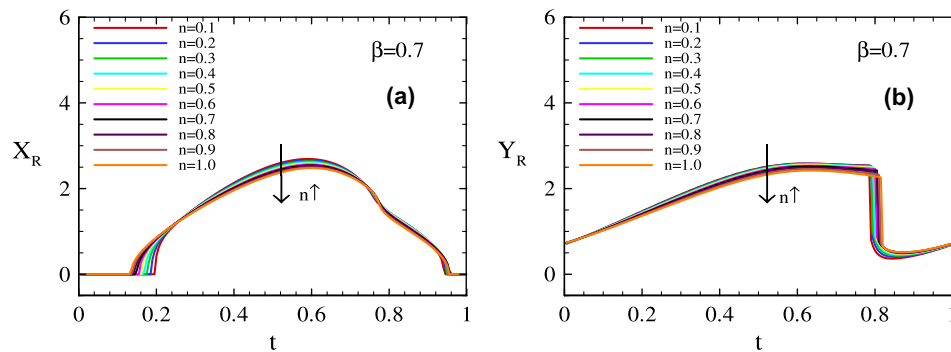


Fig. 24. Influence of shear thinning on the variation of vortex sizes,  $X_R$  (a) and  $Y_R$  (b), over a cycle, for GNF fluids (Modified Reynolds method).

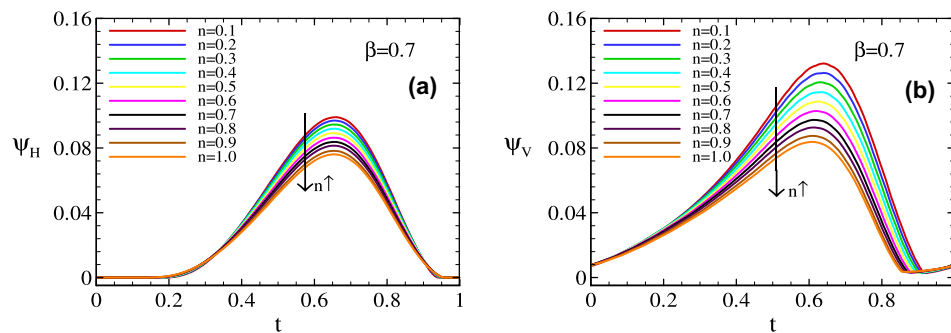


Fig. 25. Influence of shear thinning on the vortex intensities  $\psi_H$  (a) and  $\psi_V$  (b) over a cycle, for the GNF fluids (Modified Reynolds method).

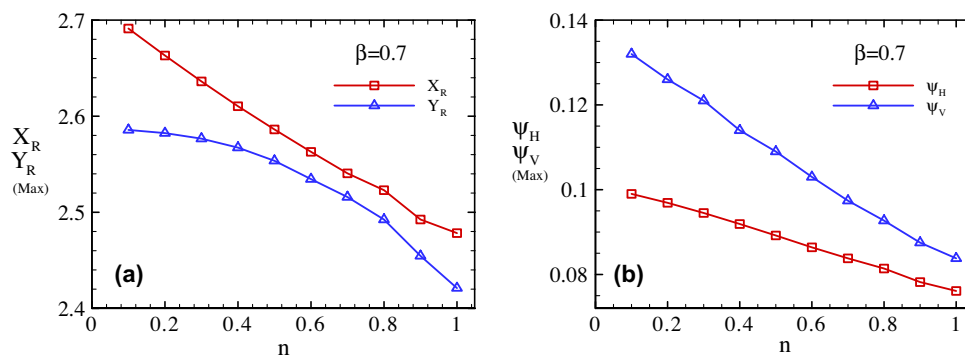


Fig. 26. Variation of the maximum sizes (a) and intensities (b) of the eddies during the cycle as a function of shear thinning ( $n = 0.3568$ ,  $Re = 102$ ).

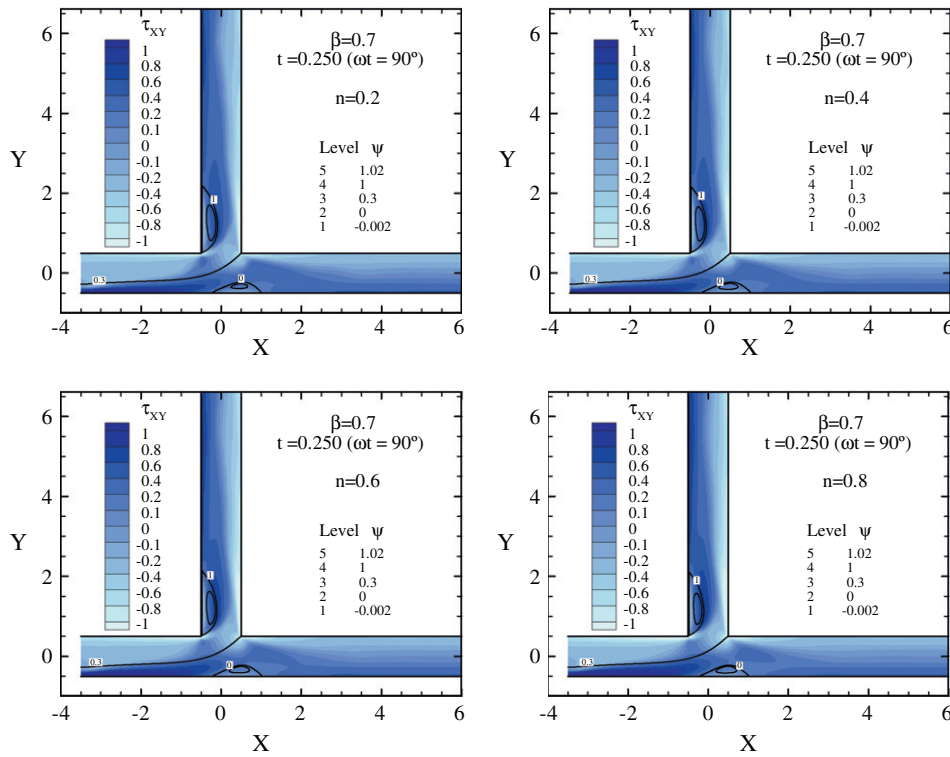


Fig. 27. Variation of shear stress field ( $\tau_{XY}$ ) with shear thinning ( $Re = 102$ ,  $\beta = 0.7$  and  $\omega t = 90^\circ$ ).

Table 8

Extreme shear stress values for the GNF fluid as a function of power law exponent, at  $\omega t = 90^\circ$  ( $\beta = 0.7$  and  $Re_{Mod} = 102$ ).

Power law index	$n = 0.1$	$n = 0.2$	$n = 0.3$	$n = 0.4$	$n = 0.5$	$n = 0.6$	$n = 0.7$	$n = 0.8$	$n = 0.9$	$n = 1.0$
Maximum shear stress ( $\tau_{XY_{Max}}/\tau_{w1}$ )	3.87	3.99	4.16	4.39	4.70	5.14	5.76	6.60	7.84	9.50
Minimum shear stress ( $\tau_{XY_{Min}}/\tau_{w1}$ )	-2.53	-2.61	-2.73	-2.87	-3.07	-3.33	-3.67	-4.12	-4.73	-5.50

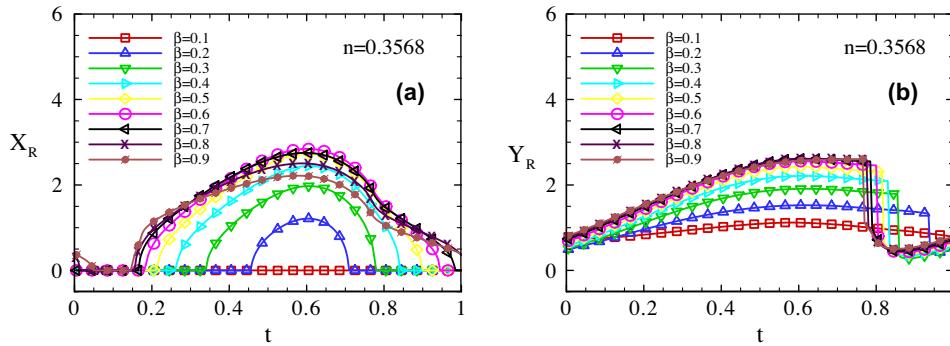


Fig. 28. Influence of extraction ratio on the cyclic variation of the eddy sizes  $X_R$  (a) and  $Y_R$  (b) for the base GNF fluid (Modified Reynolds method).

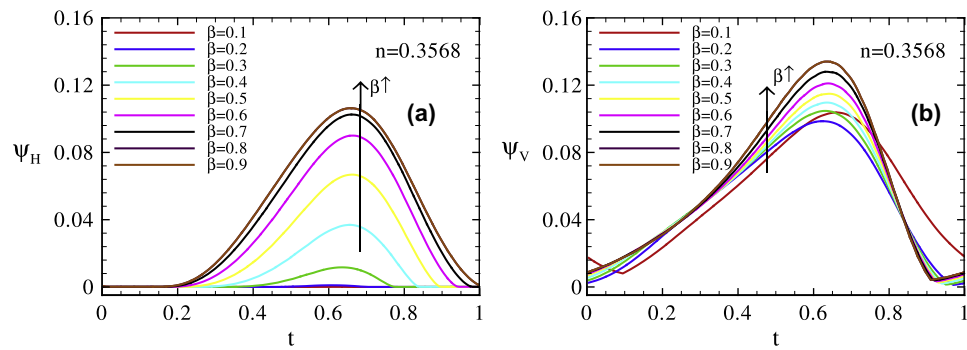
that shear-thinning in viscosity is directly proportional to the lengths and intensities of the recirculating zones formed near a  $90^\circ$  bifurcation.

Fig. 27 illustrates the influence of shear thinning on the shear stress fields in these unsteady flows. Shear stress contours are plotted after development of one quarter of the cycle ( $t = 0.25$  or  $\omega t \approx 90^\circ$ ), and for four power law exponents. As registered in the steady flows analysed before, shear thinning does not change significantly the shear stress field, except for a slight decrease in  $\tau_{XY}$  modulus with power law exponent (Table 8). Such reduction is consistent because, although there is a constancy of Reynolds number, shear-thinning promotes a local reduction of viscosity

and thus reducing the local shear stress. The maximum and minimum shear stress values for several of the shear thinning intensities investigated are registered in Table 8. There is a reduction of 59.3% in  $|\tau_{XY}|_{Max}$  when  $n$  is varied from 1 to 0.1.

### 5.2.3. Influence of extraction ratio at constant inertia and shear thinning

The flow rate ratio was varied keeping constant both the inertia ( $Re = 102$ ) and the shear thinning ( $n = 0.3568$ ), with  $Re$  based on the Modified Reynolds method. Figs. 28 and 29 display the influence of varying the flow rate ratio upon the recirculation lengths and the vortex strength, during one cycle.



**Fig. 29.** Influence of extraction ratio on the cyclic variation of the eddy intensities  $\psi_H$  (a) and  $\psi_V$  (b) for the base GNF fluid (Modified Reynolds method).

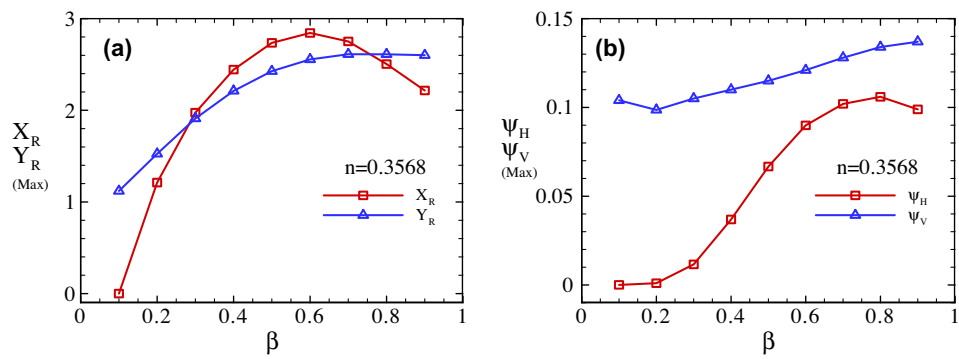


**Fig. 30.** Variation of the maximum sizes (a) and intensities (b) of the eddies during the cycle as a function of extraction ratio ( $n = 0.3568$ ,  $Re = 102$ ).

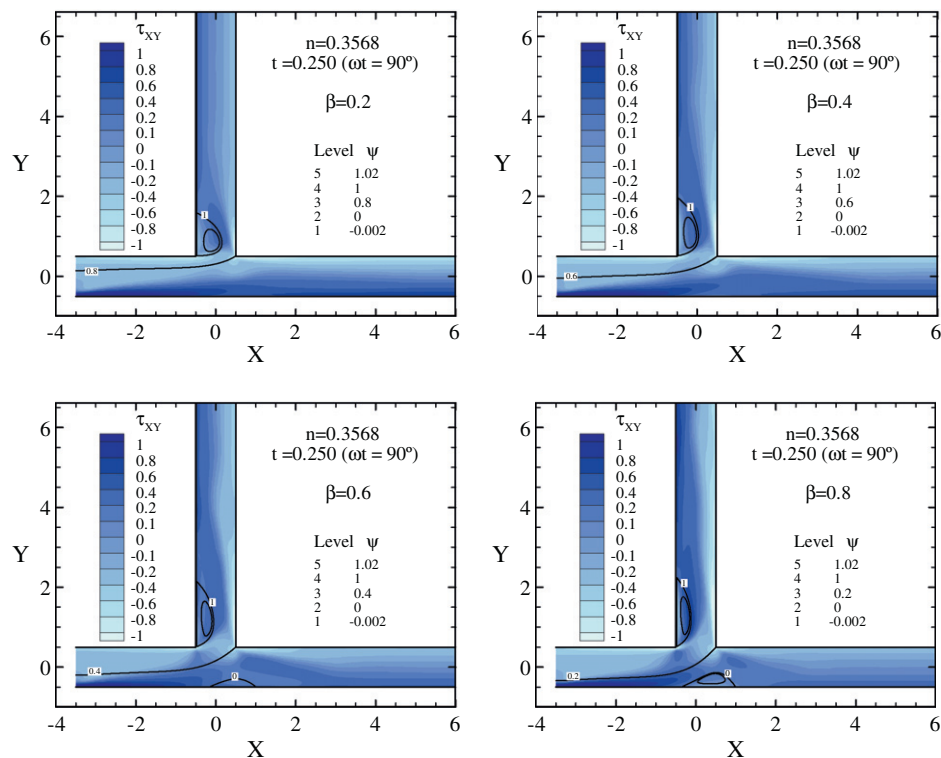


**Fig. 31.** Shear stress distribution ( $\tau_{XY}$ ) for various extraction ratios (time instant  $\omega t = 90^\circ$ ).



The horizontal recirculation length ( $X_R$ ) reaches its maximum magnitude at  $t \approx 0.6$  and  $\beta \approx 0.6$ , thus presenting a similar behaviour to what was registered for steady state flows. It tends to increase initially with the flow rate ratio, to a maximum that occurs at  $\beta \approx 0.6$ , followed by a decrease for higher flow rate ratios.

For the specific shear thinning intensity here used ( $n = 0.3568$ ) there is no recirculation in the main branch for very low flow rate ratios. The increase of flow rate ratio leads to the appearance of one eddy in the main branch which, as  $\beta$  is raised, only occurs for a short period of the cycle, but its residence time increases with flow rate ratio. This bubble exists during the entire cycle for sufficiently high flow rate ratios ( $\beta > 0.5$ ), concomitantly with small shear thinning effects.

In Fig. 28b, the vertical recirculation length is seen to increase with flow rate ratio. The rate of increase is reduced at high flow rate ratios, resulting in almost coincident  $Y_R$  versus  $t$  evolutions in these circumstances. Furthermore, the increase of flow rate ratio also tends to anticipate the division of the vertical recirculation and, for very low flow rate ratios, such division does not occur.

Fig. 29 shows the corresponding vortex intensities during the pulsating cycle for increasing flow rate ratios. The strength of the horizontal recirculation increases monotonically with flow rate ratio up to about  $\beta \leq 0.8$ , while for the vertical recirculation there is only a monotonous behaviour for flow rate ratios greater than 0.1, showing then also an increasing tendency with extraction ratio.

The different flow behaviour for the case  $\beta = 0.1$  is due to the absence of the eddy subdivision phenomenon of the vertical recirculation already discussed, which significantly affects the time evolution of the vortex strength. When the split occurs, the vortex strength of the bubble farther downstream from the bifurcation is higher than that for the bubble located immediately after the re-entrant corner (see Fig. 19). With the development of the cycle the bubble further downstream eventually disappears, at about 90% of the cycle, the vortex intensity of the bubble near the bifurcation at this instant is larger than the other splitted bubble, and it starts increasing in size and vorticity again. With  $\beta = 0.1$  the abrupt reduction of the vortex does not occur and the length and intensity of the recirculation reach their minimum values at about 10% of the cycle, explaining the differences for this case in Fig. 29.

Fig. 30 quantifies and makes it clear how the maximum sizes of the two recirculating zones ( $X_R$  and  $Y_R$ ) and their maximum intensities ( $\psi_H$  and  $\psi_V$ ) vary as  $\beta$  is increased. These data correspond to the maximum values in Figs. 28 and 29. While the side-branch eddy attains maximum size and intensity that raise monotonically with  $\beta$ , as expected since increasing  $\beta$  corresponds to increasing the effective  $Re$  in the branch, the main channel eddy attains maximum size at  $\beta = 0.6$  and intensity at  $\beta = 0.8$ .

Fig. 31 shows the influence of the flow rate ratio upon the shear stress fields, for unsteady flows, with in general a behaviour similar to that registered earlier for steady state flows. For low flow rate ratios the shear stress field presents higher magnitudes along the main channel after the bifurcation, which decrease when the flow rate ratio increases. On the other hand, in the secondary channel there is an opposite effect and the shear stresses increase with flow rate ratio, with the higher magnitudes being located in this branch at large flow rate ratios. Regardless of their location the maximum magnitude of shear stress tends to increase with flow rate ratio.

## 6. Conclusions

In the present paper we have carried out a numerical study of two-dimensional bifurcating flows with non-Newtonian fluids whose characteristics for the base case are similar to blood, therefore being a study with relevance to hemodynamics. In particular, we looked to the eddy lengths and intensities and to the shear stress fields within the flow domain and on the walls, for both steady

and unsteady flow conditions, and for different power-law indices and extraction ratio values. Such a study is important to hemodynamics since the inception and development of atherosclerotic diseases are frequently correlated with the existence of flow separation and recirculations, and with low or oscillating shear stresses, like those occurring in bifurcation flows similar to the ones here considered. In addition the present work also clarifies the use of the definition for the Reynolds number, which may be calculated using Newtonian conditions or, more consistently, taking into account the non-Newtonian nature of the fluids, in which the viscosity changes with shear rate.

The first conclusion is that proper account of shear thinning effects on the viscosity used to define the Reynolds number is required for comparison between several cases at the same level of inertia. This is also true when the power-law index is varied and, if one is not careful, the cases compared would exhibit different inertia. This we believe is a very important conclusion when comparing Newtonian and non-Newtonian GNF simulations, even if the degree of agreement here attained is not perfect and depends on  $n$  and  $\beta$ . The effective Reynolds number defined in Section 4 is based on global characteristics defining a shear rate at inlet, and cannot of course imply a perfect match of local flow features in the junction zone. Other choices for the characteristic  $\dot{\gamma}$  are possible, for example  $\dot{\gamma} = \sqrt{(\bar{u}_2/H_2)^2 + (\bar{u}_3/H_3)^2} = \dot{\gamma}_1 \sqrt{(1-\beta)^2 + \beta^2}$  (when all ducts have the same width  $H$ ). Such choices need to be carefully evaluated, a matter beyond the scope of the present work.

A second conclusion that the present results show is that the GNF fluids tend to present longer recirculation lengths in the main and the side branches and reduced shear stress field magnitudes when compared to corresponding (same inertia) Newtonian flows. However the influence of shear thinning does not present a monotonous behaviour for the steady state flows. On the other hand, for unsteady flows the behaviour is monotonous and almost linear (except  $Y_R$ ), with decreasing recirculation lengths and increasing shear stress magnitudes as the power law exponent is increased (reduced shear thinning).

Inertia, as measured by a Reynolds number, presents a monotonous behaviour, leading to an increase of the vortex intensities and sizes, for both recirculating bubbles, as well as of the shear stress magnitudes.

Flow rate ratio, for both steady and unsteady flows, does not exhibit a monotonous behaviour. In steady state flows, the recirculation lengths increase with flow rate ratio for all Reynolds numbers, up to maximum values at  $\beta = 0.6$ , and decrease after that. On the other hand for unsteady flows this behaviour only occurs for a specific time gap in the middle of the cycle, and mainly so for the horizontal recirculation length ( $X_R$ ) that reaches the maximum magnitude at around  $\beta = 0.6$ , lasting about 30% of the cycle, while the vertical recirculation attains a maximum at  $\beta = 0.7$ , and only for a very short period of time. In the remaining duration of the cycle there is a monotonous behaviour with recirculation lengths increasing with flow rate ratio. In general the vortex strength of both recirculations increases with flow rate ratio for steady and unsteady flows, with the exception of low Reynolds number cases ( $Re < 200$ ) in steady state flows where the behaviour is opposite. For both fluid types (Newtonian and GNF) the maximum magnitudes of shear stress increase with flow rate ratio, and their location changes; for small extraction ratios, they occur in the main branch, where larger amount of fluid is then present and larger stretching occurs, while for higher ratios they occur in the secondary branch.

For unsteady flows the various vortex characteristics change over the cycle. The recirculation lengths and vortex strengths increase up to a maximum at about 60% of the cycle and decrease after that. The horizontal recirculation does not always exist during

the entire cycle and the residence time increases with power law exponent and flow rate ratio. For the vertical recirculation there is a vortex subdivision of the main eddy at about 80% of the cycle, and the second eddy tends to disappear as the cycle develops (it is carried along by the branch flow). An increase of shear thinning and flow rate ratio results in early division of the main vertical recirculation, which does not occur for very low flow rate ratios.

Future work will need to consider the 3D nature of the flow, especially when the aspect ratio of the actual rectangular cross-section of the ducts forming the T-junction is smaller than about 8 (depth/height), the value used in the experiments of Khodadadi et al. (1988). In the unsteady state simulations, even for 2D, there is the need of further checking the influence of varying the frequency of the imposed pressure gradient.

## References

- Alves, M.A., Oliveira, P.J., Pinho, F.T., 2003. A convergent and universally bounded interpolation scheme for the treatment of advection. *Int. J. Numer. Meth. Fluids* 41, 47–75.
- Balan, C.M., Broboana, D., Balan, C., 2010. Mixing process of immiscible fluids in microchannels. *Int. J. Heat Fluid Flow* 31, 1125–1133.
- Banerjee, R.K., Cho, Y.I., Kensey, K.R., 1997. A study of local hydrodynamics in a 90 branched vessel with extreme pulsatile flows. *Int. J. Comput. Fluid Dyn.* 9, 23–42.
- Berger, S.A., Jou, L.-D., 2000. Flows in stenotic vessels. *Annu. Rev. Fluid Mech.* 32, 347–382.
- Caro, C.G., Fitz-Gerald, J.M., Schroter, R.C., 1971. Atheroma and arterial wall shear. Observation, correlation and proposal of a shear dependent mass transfer mechanism for atherogenesis. *Proc. R. Soc. Lond. B. Biol. Sci.* B177 (1046), 109–159.
- Chien, S., 2008. Effects of disturbed flow on endothelial cells. *Ann. Biomed. Eng.* 36, 554–562.
- Chitra, K., Vengadesan, S., Sundararajan, T., Nithiarasu, P., 2009. An investigation of pulsatile flow in a model cavo-pulmonary vascular system. *Commun. Numer. Methods Eng.* 25, 1061–1083.
- Cho, Y.I., Kensey, K.R., 1991. Effects of the non-Newtonian viscosity of blood on flows in a dissected arterial vessel: Part 1. Steady flows. *Biorheology* 28, 241–262.
- Costa, N.P., Maia, R., Pinho, F.T., Proença, M.F., 2006. Edge effects on the flow characteristics in a 90° tee junction. *J. Fluids Eng.* 128, 1204–1217.
- Crowther, M.A., 2005. Pathogenesis of atherosclerosis. *Hematology (Am Soc Hematol Educ Program)* 1, 436–441.
- Cunningham, K.S., Gotlieb, A.I., 2005. The role of shear stress in the pathogenesis of atherosclerosis. *Lab. Invest.* 85, 9–23.
- de Backer, G., Ambrosioni, E., Borch-Johnsen, K., et al., 2003. European guidelines on cardiovascular disease prevention in clinical practice. *Eur. Heart J.* 24, 1601–1610.
- Debaek, M.E., Lawrie, G.M., Glaeser, D.H., 1985. Patterns of atherosclerosis and their surgical significance. *Ann. Surg.* 201, 115–131.
- Doherty, A.P., Murphy, A., Spedding, P.L., 2009. Fluid flow in an impacting symmetrical tee junction II: two-phase air/water flow. *Asia-Pac. J. Chem. Eng.* 4, 424–431.
- Escudier, M.P., Oliveira, P.J., Pinho, F.T., Smith, S., 2002. Fully-developed laminar flow of non-Newtonian liquids through annuli: comparison of numerical calculations with experiments. *Exp. Fluids* 33, 101–111.
- Ferziger, J.H., Peric, M., 2002. *Computational Methods for Fluid Dynamics*, 3rd ed. Springer Verlag.
- Fry, D.L., 1969. Certain histological and chemical responses of the vascular interface to acutely induced mechanical stress in the aorta of the dog. *Circ. Res.* 24, 93–108.
- Gray, J.D., Owen, I., Escudier, M.P., 2007. Dynamic scaling of unsteady shear-thinning non-Newtonian fluid flows in a large-scale model of a distal anastomosis. *Exp. Fluids* 43, 535–546.
- Hsiai, T., Cho, S., Wong, P., Ing, M., Salazar, A., Sevanian, A., Navab, M., et al., 2003. Monocyte recruitment to endothelial cells in response to oscillatory shear stress. *FASEB J.* 17, 1648–1657.
- Issa, R.I., Oliveira, P.J., 1994. Numerical prediction of phase-separation in two-phase flow through T-junctions. *Comput. Fluids* 23, 347–372.
- Joris, E., Zand, T., Majno, G., 1982. Hydrodynamic injury of the endothelium in acute aortic stenosis. *Am. J. Pathol.* 106, 394–408.
- Ku, D.N., Giddens, D.P., Zarins, C.K., Glagov, S., 1985. Pulsatile flow and atherosclerosis in the human carotid bifurcation. Positive correlation between plaque location and low oscillating shear stress. *Atherosclerosis* 5, 293–302.
- Khodadadi, J.M., Nguyen, T.M., Vlachos, N.S., 1986. Laminar forced convective heat transfer in a two-dimensional 90° bifurcation. *Numer. Heat Transfer* 9, 677–695.
- Khodadadi, J.M., Vlachos, N.S., Liepsch, D., Moravec, S., 1988. LDA measurements and numerical prediction of pulsatile laminar flow in a 90-degree bifurcation. *J. Biomech. Eng.* 110, 129–136.
- Khodadadi, J.M., 1991. Wall pressure and shear stress variations in a 90-Deg bifurcation during pulsatile laminar flow. *J. Fluids Eng.* 113, 111–115.
- Liepsch, D., Moravec, S., Rastogi, A.K., Vlachos, N.S., 1982. Measurement and calculations of laminar flow in a ninety degree bifurcation. *J. Biomech.* 15, 473–485.
- Long, J.A., Ündar, A., Manning, K.B., Deutsch, S., 2005. Viscoelasticity of pediatric blood and its implications for the testing of a pulsatile pediatric blood pump. *ASAIO J.* 51, 563–566.
- Louda, P., Kozel, K., Přihoda, J., Beneš, L., Kopáček, T., 2011. Numerical solution of incompressible flow through branched channels. *Comput. Fluids* 46, 318–324.
- Matos, H.M., Alves, M.A., Oliveira, P.J., 2009. New formulation for stress calculation: application to viscoelastic flow in a T-junction. *Numer. Heat Transfer B-Fund.* 56, 351–371.
- Miranda, A.I.P., Oliveira, P.J., Pinho, F.T., 2008. Steady and unsteady laminar flows of Newtonian and generalized Newtonian fluids in a planar T-junction. *Int. J. Numer. Meth. Fluids* 57, 295–328.
- Moshkin, N., Yambangwi, D., 2009. Steady viscous incompressible flow driven by a pressure difference in a planar T-junction channel. *Int. J. Comput. Fluid Dyn.* 23, 259–270.
- Neary, V.S., Sotiropoulos, F., 1996. Numerical investigation of laminar flows through 90-degree diversions of rectangular cross-section. *Comput. Fluids* 25, 95–118.
- Neary, V.S., Sotiropoulos, F., Odgaard, A.J., 1999. Three-dimensional numerical model of lateral-intake inflows. *J. Hydraul. Eng.* 125, 126–140.
- Oliveira, P.J., Pinho, F.T., Pinto, G.A., 1998. Numerical simulation of non-linear flows with a general collocated finite-volume method. *J. Non-Newton. Fluid Mech.* 79, 1–43.
- Oliveira, P.J., Pinho, F.T., 1999. Numerical procedure for the computation of fluid flow with arbitrary stress-strain relationships. *Numer. Heat Transfer B-Fund.* 35, 295–315.
- Oliveira, P.J., 2001. Method for time-dependent simulations of viscoelastic flows: vortex shedding behind cylinder. *J. Non-Newton. Fluid Mech.* 101, 113–137.
- Owens, R.G., 2006. A new microstructure-based constitutive model for human blood. *J. Non-Newtonian Fluid Mech.* 140, 57–70.
- Rhie, C.M., Chow, W.L., 1983. Numerical study of the turbulent flow past an airfoil with trailing edge separation. *AIAA J.* 21, 1525–1532.
- Ross, R., 1999. Atherosclerosis – an inflammatory disease. *New Engl. J. Med.* 340, 115–126.
- Shah, R.K., London, A.L., 1978. *Laminar Flow Forced Convection in Ducts*. Academic Press, New York.
- Stuart, J., Kenny, M.W., 1980. Blood rheology. *J. Clin. Pathol.* 33, 417–429.
- Tsui, Y.-Y., Lu, C.-Y., 2006. A study of the recirculating flow in planar, symmetrical branching channels. *Int. J. Numer. Meth. Fluids* 50, 235–253.
- Van Doormaal, J.P., Raithby, G.D., 1984. Enhancements of the SIMPLE method for predicting incompressible fluid flows. *Numer. Heat Transfer* 7, 147–163.
- Yasuda, K., Armstrong, R.C., Cohen, R.E., 1981. Shear-flow properties of concentrated solutions of linear and branched polystyrenes. *Rheol. Acta* 20, 163–178.
- Zarins, C.K., Giddens, D.P., Bharadvaj, B.K., Sottiurai, V.S., Mabon, R.F., Glagov, S., 1983. Carotid bifurcation atherosclerosis. Quantitative correlation of plaque localization with flow velocity profiles and wall shear stress. *Circ. Res.* 53, 502–514.